Ambient Noise Tomography of Northeastern China, the Korean Peninsula, and the Sea of Japan

Yong Zheng[1], Weisen Shen[2], Longquan Zhou[4], Yingjie Yang[1,3], Zujun Xie[1], and Michael H. Ritzwoller[2]

1. Key Laboratory of Dynamic Geodesy, Institute of Geodesy and Geophysics, Chinese Academy of Sciences, Wuhan, Hubei, 430077, China (zhengyong@whigg.ac.cn)
2. Center for Imaging the Earth's Interior, Department of Physics, University of Colorado at Boulder, Boulder, CO 80309-0390 (michael.ritzwoller@colorado.edu)
3. Department of Earth and Planetary Sciences, Macquarie University, 2109 Sydney Australia (yingjie.yang@mq.edu.au)
4. China Earthquake Network Center, Beijing, 100045, China (lqzhou@seis.ac.cn)

Abstract:

This study lays the foundation for a high-resolution 3-D model of the crust and uppermost mantle to a depth of about 80 km beneath northeastern China and surrounding regions. Such a model is motivated to produce new constraints on the massive volcanism, crustal extension, cratonic rejuvenation, and lithospheric thinning that are hypothesized for northeastern China. Ambient noise tomography is particularly needed to constrain the structure of the crust, and complements information from other types of data. Ambient noise tomography is applied here to data from more than 300 broad-band seismic stations from Chinese Provincial networks, the Japanese F-Net, and the IRIS Global Seismic Network, producing more than 50,000 inter-station paths across the region. Two years of continuous data from 2007 into 2009 are used to produce group and phase velocity maps from 12 sec to 45 sec period across northeastern China, the Korean Peninsula, and the Sea of Japan. To generate the Rayleigh wave dispersion maps, the effects of the persistent localized Kyushu microseism were eliminated in the dispersion measurements. In doing so, the location of the microseism by Zeng and Ni (2010) is confirmed. Average resolution across the study region is estimated to be about 100 km. The dispersion maps are geologically coherent, displaying the signatures of a variety of crustal structures, including sedimentary basins, mountain roots, ocean-continent variations, and anomalies due to continental rifting and volcanism. The maps at different periods and between phase and group velocities are consistent with one another, and vertically relatively smooth Vs models are shown fit the observations well.

Keywords Ambient noise, surface wave dispersion, Rayleigh waves, Sea of Japan, North China, Kyushu microseism

Submitted to *Journal of Geophysical Research*, June, 2011

1. Introduction

The goal of this study and a companion paper by Zhou et al. (2011) is to advance toward an integrated, highly resolved shear wave speed (Vs) model of the crust and uppermost mantle beneath all of East China. Zhou et al. (2011) focus on Southeast China. The complementary focus of the current paper is northeastern China, the Korean Peninsula, and the Sea of Japan. More than 320 seismic stations from Chinese provincial networks in northeastern China and surrounding areas, Japanese F-Net stations (Okada et al., 2004), and IRIS GSN stations are the basis for this study (Fig. 1). The resulting station and path coverage that emerges is unprecedented in this region. In order to place strong constraints on crustal structure, ambient noise tomography is employed. As described below, ambient noise tomography has already been employed in other regions of China (e.g., Tibet), at larger scales (e.g., across all of China) at a lower resolution, or in a part of the study region (e.g., North China platform, Korean peninsula), but a resulting integrated, high resolution model of all of northeastern China has been elusive. Such a model is desired to illuminate a set of interconnected tectonic problems that make northeastern China a particularly fertile area for seismic tomography.

Northeastern China is composed of a mosaic of tectonic blocks and lineated orogenic belts (Fig. 2) that have been arranged and modified by a long, complex, and in some cases enigmatic history of subduction, accretion, and collision dating back to the Archean (e.g., Zhang et al., 1984). In the south, the wedge-shaped Sino-Korean Craton (SKC), delineated by red lines in Figure 2, is separated from the Yangtze Craton by the Qinling-Dabie-Sulu orogenic belt. The SKC itself consists of the Ordos Block, the North China platform, at least parts of the East Shandong-Yellow Sea Block, as well as marginal and intruding mountain ranges. North of the SKC, the Xing'an-East Mongolia block is separated from the Songliao-Bohai graben by the North-South Gravity Lineament (NSGL). The NSGL extends southward into the SKC near the western edge of the North China Platform. The Songliao-Bohai graben, stretching from the Songliao basin to the Bohai Gulf, is flanked to east by the Tancheng-Lujiang (Tanlu) Fault that

extends into the SKC and forms the eastern boundary of the North China Platform. The Tanlu Fault also defines the western border of the Northeast Asia Foldbelt.

Much of northeastern China has undergone extensive tectonism during the late Mesozonic and Cenozoic eras (e.g., Yin, 2010). Northeastern China, bounded by the SKC to the south and the Sea of Japan backarc basin to the east, is part of eastern China's Cenozoic volcanic zone (e.g, Ren et al., 2002). Episodic volcanism has been particularly prominent along three volcanic mountain chains (Great Xing'an Range (GXAR), Lesser Xing'an Range (LXAR), Changbaishan (CBM)) and apparently has been linked competitively throughout the Cenozoic to the opening of the Sea of Japan (Liu et al., 2001). Rifting and extension are believed to have begun in the late Mesozoic (Tian et al., 1992) and have led to the development of the Songliao basin, although the Songliao basement is traced back to the Archean (Rogers and Santosh, 2006). The SKC formed largely in the Archean, but it is a paradigm of an Archean craton that has lost its lithospheric keel. Petrological and geochemical evidence (e.g., Menzies et al., 1993; Griffin et al., 1998) suggests that typical cratonic lithosphere existed beneath the entire SKC until the Mesozoic era when the SKC was reactivated and lithospheric thinning occurred at least beneath the North China platform.

The physical mechanisms that have produced the massive volcanism, crustal extension, cratonic rejuvenation and lithospheric thinning that have occurred across parts of northeastern China remain poorly understood (Deng et al., 2007). For example, changes in both lithospheric rheology ("bottom up") and density ("top down") have been hypothesized to govern the lithospheric thinning of the eastern SKC (Menzies et al., 2007). On the one hand, the generally slow processes of lithospheric basal thermal erosion, chemical metasomatism (Gao et al., 2008), and volatile enrichment (e.g., Richard and Iwamori, 2010) have been hypothesized to transform the lower lithospheric mantle to asthenosphere. In contrast, much faster delamination of the lower part of the lithospheric mantle or the entire lithospheric mantle including the lower crust

(e.g., Gao et al., 2004; Zhai et al., 2007) has also been hypothesized, which depends on density. As another example, the physical linkage between the coupled, sequential openings of the Songliao graben (e.g., Liu et al., 2001) and the Sea of Japan (Tatsumi et al., 1989; Jolivet et al., 1994) remains poorly understood.

These questions can be illuminated with seismic images of velocity heterogeneities, internal discontinuities, and crustal and mantle anisotropy, yet the vast majority of the studies to date have been geochemical or petrological in nature. Increasingly, seismological studies are adding new information due in part to the rapid expansion of seismic instrumentation in China over the past few years (e.g., Zheng et al., 2010a). These studies include body wave tomography of the mantle (e.g., Lebedev and Nolet, 2003; Huang and Zhao, 2006; Zhao, 2009; Tian et al., 2009; Xu and Zhao, 2009; Li and van der Hilst, 2010; Santosh et al., 2010) and of the crust (e.g., Sun and Toksoz, 2006). Pn tomography (Li et al., 2011), receiver functions analyses (Zheng et al., 2006; Chen et al., 2009), and shear wave splitting studies have also been performed (Zhao et al., 2008; Bai et al., 2010; Li and Niu, 2010). Recent body wave results have focused mainly on the eastern SKC (N. China platform) and include imaging the thin lithosphere beneath the eastern SKC as well as the potential remnants of the delaminated lithosphere near 400 km depth (e.g., Chen et al., 2009; Xu and Zhao, 2009).

At least parts of northeast China have been imaged by larger scale teleseismic surface wave dispersion studies (e.g., Ritzwoller and Levshin, 1998; Ritzwoller et al., 1998; Villaseñor et al., 2001; Yanovskaya and Kozhevnikov, 2003; Huang et al., 2003, 2004; Priestley et al., 2006). Recent regional scale teleseismic surface wave studies have also been conducted within North China (e.g., Tang and Chen, 2008; Huang et al., 2009; Zhou et al., 2009; He et al., 2009; Pan et al., 2011), in adjacent regions (e.g., Yao et al., 2006, 2008), and in the Sea of Japan (e.g., Bourova et al., 2010; Yoshizawa et al, 2010).

Within the last few years a new method of surface wave tomography has emerged based on using

ambient seismic noise to extract surface wave empirical Green's functions (EGFs) and to infer Rayleigh (e.g., Sabra et al., 2005; Shapiro et al., 2005) and Love wave (e.g., Lin et al., 2008) group and phase speeds in continental areas. Compared with traditional earthquake tomography methods, ambient noise tomography is free from artifacts related to the distribution of earthquakes as well as errors in earthquake locations and source mechanisms. The dominant frequency band of the ambient noise lies between about 8 and 40 sec period. Rayleigh waves in this band are sensitive to crustal and uppermost mantle structures. Ambient noise tomography has produced phase and group velocity maps in various regions around the world (e.g., Moschetti et al., 2007; Yang et al., 2007; Bensen et al., 2008) and also is the basis for 3-D crustal and uppermost mantle models of isotropic shear velocity structure (e.g., Yang et al., 2008a, 2008b; Bensen et al., 2009; Moschetti et al., 2010b), radial anisotropy (e.g., Moschetti et al., 2010a), and azimuthal anisotropy (e.g., Lin et al., 2011). Ambient noise in east Asia has been shown to be sufficiently well distributed in azimuthal content to be used for surface wave dispersion measurements (e.g., Yang and Ritzwoller, 2008) and studies based on ambient noise have been conducted at large scales across all of China (Zheng et al., 2008; Sun et al., 2010), in regions adjacent to northeastern China (e.g., Yao et al., 2006, 2008; Guo et al., 2009; Li et al., 2009; Huang et al., 2010; Yang et al., 2010; Zheng et al., 2010b; Zhou et al., 2011), within the North China Platform (Fang et al., 2010); on the Korean Peninsula (Kang and Shin, 2006; Cho et al., 2007), and in Japan (e.g., Nishida et al., 2008).

Ambient noise tomography in northeastern China and the Sea of Japan, however, is faced with an uncommon technical challenge – the existence of a persistent localized microseismic source near Kyushu Island (Zeng and Ni, 2010) in the period band between about 8 and 14 sec. This signal causes a significant disturbance that is observable on cross-correlations of ambient noise, which, if left uncorrected, would bias measurements of group and phase velocity in this period band of considerable sensitivity to upper crustal structure. A defining focus of this paper, therefore, is to identify this disturbance and minimize its effects on the estimated Rayleigh wave group and

phase velocity dispersion maps.

The present paper takes a major step toward developing a 3-D Vs model of the study region by presenting Rayleigh wave group and phase velocity maps from 10 to 40 sec period. The resulting information complements existing and emerging teleseismic body wave and surface studies by presenting new and much stronger constraints on the structure of the crust and uppermost mantle lithosphere. The construction of a 3-D model is beyond the scope of the present paper, but local 1-D models constructed by Monte-Carlo inversion are presented to illuminate the dispersion maps. The data processing and quality control procedures are described in section 2 and methods used to de-sensitize the data to degradation caused by the persistent, localized Kyushu microseism are presented in section 3. The Rayleigh wave group and phase velocity maps are described in sections 4 and 5. Section 5 also presents the set of 1-D Vs models across the study region.

2. Data Processing and Quality Control

The data used in this study are continuous seismic waveforms recorded at broadband stations that existed in and around northeast China and the Sea of Japan from August 2007 to July 2009. Networks providing data include: (1) Chinese Provincial Networks in northeast China consisting of 232 broadband seismic stations, (2) F-Net in Japan comprising 69 long period seismic stations, and (3) the IRIS GSN broadband network in northeast Asia consisting of 22 stations. In total, two years of continuous waveform data have been acquired that were recorded at the 323 stations denoted by solid triangles and squares in Figure 1. Only vertical component data are processed, meaning only Rayleigh waves are studied.

The data processing procedures follow those of Bensen et al. (2007) and Lin et al. (2008). After removing the instrument responses, all records are bandpass filtered between 5 and 150 sec period. We apply both temporal normalization and spectral whitening. Temporal normalization is applied in an 80 second moving window. Cross-correlations are performed daily between all

pairs of stations in the period band from 5-50 sec and then are stacked over the two-year time window.

Figure 3a-c presents example cross-correlation record sections among Chinese stations, among F-Net stations, and inter-station pairs between F-Net stations and Chinese stations.

Data quality control is discussed here and in section 3 and consists of five principal steps, denoted A-E. Most of these steps are based on procedures summarized by Bensen et al. (2007) and Lin et al. (2008), but because of the mixture of instrument types used in this study and the existence of the Kyushu microseism we add extra steps to ensure the reliability of the resulting dispersion measurements. Step A. A dispersion measurement is retained for a cross-correlation at a given period only if signal-to-noise ratio (SNR) > 15 at that period, where SNR is defined by Bensen et al. (2007). Step B. We remove the effects of the Kyushu microseism, which we discuss further in section 3. Step C. We retain an observation at a given period only if both the group and phase velocities are measured by the automated frequency-time analysis method (Bensen et al., 2007). Group and phase velocity are separate measurements and are not constrained to agree even though they are related theoretically (e.g., Levshin et al., 1999). Step D. We identify and discard stations with bad instrument responses. Step E. This step is broken into two parts. First, we only accept dispersion measurements with path lengths $\geq$ 3 wavelengths. Second, a measurement is retained only if the misfit determined from the final dispersion map is less than 12 sec for group travel time and less than 5 sec for phase travel time, which is somewhat more than twice the standard deviation of the final misfit. Group and phase velocity dispersion measurements of Rayleigh waves are obtained on the symmetric component of inter-station cross-correlations except for paths identified as affected by the Kyushu microseism, as discussed further in section 3.

Because the seismic instruments used in this study differ in origin between China, Japan, and the US, and instruments can vary between provinces in China, it is important to identify errors and

inconsistencies in response files. For the IRIS network data, F-Net data and most of the Chinese stations, full response (RESP) files including both analog and digital filter stages are available. For a small number of Chinese stations only pole-zero response files missing the digital filtering stages exist. We find that for the Chinese instruments, the analog pole-zero responses may differ from the full responses computed from the RESP files for stations that have both types of response files. Therefore, we discard the Chinese stations for which we have not been able to acquire RESP files. This affected 36 stations, but none are included in the 232 Chinese stations shown in Figure 1. Using these response files, all data are converted to velocity prior to cross-correlation.

Two other procedures are applied to find other instrument response errors. First, we identify polarity errors (π phase shift) that may represent a units error in the instrument by comparing P-wave first motions observed across the array following deep, distant teleseisms. We also look for half-period misfits based on the final tomography maps at each period. These procedures identified seven stations with polarity errors that are discarded. Second, we compare the phase and group times measured on the positive and negative lags of all cross-correlations, which identifies timing errors as long as both lags have a high SNR (Lin et al., 2007). These procedures identified and discarded three Chinese stations.

The 2π phase ambiguity inherent in phase velocity measurements is resolved iteratively, first based on phase velocities predicted by the 3D model of Shapiro et al. (2002) and then later on increasingly refined phase velocity maps that are determined in this study.

With more than 300 stations, in principal about 50,000 inter-station cross-correlations could be obtained. Quality control procedures reduce this number appreciably as Table 1 shows. The SNR criterion (Step A) removes between 1/3 and 2/3 of the measurements, with the greatest loss being at long periods ($\geq$ 30 sec). Step B, the removal of the effect of the Kyushu signal (described in section 3), also removes a large number of measurements. Around 23% of dispersion

measurements at 12 sec period and 18% of measurements at 14 sec period are removed. Because the disturbance decreases with increasing period, however, the rejected percentage decreases gradually from 14 sec period to 18 sec period. No measurements are removed above 18 sec period. In Step E, the 5 sec phase time and the 12 sec group time acceptance criteria reject ~10% of measurements at most periods. After applying these criteria, we obtain between ~15,000 to 30,00 group and phase velocity measurements for tomography at periods ranging from 10 to 40 sec. This number maximizes between 20 and 25 sec period. This number is suitable to produce relatively high-resolution group and phase maps across most of northeastern China and the Sea of Japan.

3. The Effect of the Localized Persistent Kyushu Microseism

In northeast China, a strong disturbance appears on the cross-correlation waveforms. The record sections shown in Figures 3b and 3c show this disturbance, which appears as precursory signals (identified by white dots) in addition to the expected surface wave part of the empirical Green's function. Another example is presented in Figure 4a, where the disturbance appears between 100 and 150 sec, whereas the desired Rayleigh wave signal arrives much later and is seen clearly at negative correlation lag. The arrival of these disturbances near to the Rayleigh wave wavepackets interferes with the ability to measure Rayleigh wave speeds accurately. In fact, as we show here, the effect tends to bias Rayleigh waves fast, particularly for Rayleigh wave group velocities.

These precursory signals are due to the persistent, localized Kyushu microseism that has been identified by Zeng and Ni (2010), who located it near the island of Kyushu, Japan, within our study region. The period band of this microseism is dominantly between 8 and 14 sec. The physical nature and cause of this microseism remain unknown, but it is reminiscent of the longer period persistent 26 sec microseism located in the Gulf of Guinea (e.g., Shapiro et al., 2006). We are interested in minimizing its interference with surface wave dispersion measurements across

the study region. To do so, we have re-located it, confirming the location of Zeng and Ni (2010), and have developed a data processing procedure that allows reliable dispersion curves to be obtained across northeastern China, the Korean peninsula, and the Sea of Japan. The effect of the procedure, however, is to reduce the number of measurements in the region broadly surrounding Kyushu at periods between 10 and 18 sec.

3.1 Re-location of the Kyushu microseism

We use the envelope functions between periods of 10 and 12 sec for the Kyushu signal observed on inter-station cross-correlations to locate the Kyushu microseism. An example envelope function is shown in the bottom panel of Figure 4a. Based on an initial observed group velocity map at 11 sec period, we predict the theoretical arrival time of the Kyushu signal for each inter-station pair for each hypothetical source location on a broad map of the region. We then take the observed amplitude of the envelope function at the predicted time and plot it at the hypothetical source location. An example is shown in Figure 4b, where the hyperbola identifies the set of possible locations for the Kyushu microseism for a particular inter-station pair. We refer to this figure as the migrated envelope function. Finally, we stack over all migrated envelope functions for cross-correlations involving the GSN stations INCN (Inchon, South Korea) and SSE (Shanghai, China), with the paths shown in Figure 4c. The resulting stack of migrated envelope functions is shown in Figure 4d, demonstrating that the re-location of the Kyushu microseism is close to the location from Zeng and Ni (2010) (Fig. 4d).

Because the physical mechanism of the microseism is not understood, we have no reason to believe that it is a point source. However, the present analysis is consistent with it being a point source. Further analysis of the duration of the microseismic envelope function is needed to advance this analysis.

3.2 Eliminating the effect of the Kyushu microseism

Assuming that the Kyushu microseism is a point source, for each inter-station cross-correlation we calculate the expected arrival time of the Kyushu signal as well as the theoretical arrival time of the Rayleigh wave between the two-stations. As Figures 5a and 5b show, the relative arrival times of the Kyushu signal (white dots) and the inter-station Rayleigh wave (blue dots) are highly variable but systematic. For example, in Figure 5a, which displays cross-correlations between the South Korean GSN station (INCN) and F-Net stations in Japan, the Kyushu signal is well separated from the inter-station Rayleigh wave as long as inter-station path lengths are longer than ~800km. However, the arrival times of the Kyushu signals are close to the surface waves on the negative components of the cross-correlations between INCN and Chinese stations (Fig. 5b). The paths from station INCN that would be affected by the Kyushu signal are shown as red lines in Figure 5c. On these paths it would be very difficult to separate the signals between 8 and 14 sec period on the symmetric component of the cross-correlation. However, the systematics of the relative arrival times can be exploited to separate the two waves and obtain reliable Rayleigh wave group and phase velocity measurements for most paths by focusing on a single correlation lag.

Figure 6 illustrates how the Kyushu signal biases group and phase velocity measurements when the Rayleigh wave and the Kyushu signal arrive nearly simultaneously on the negative lag component of the cross-correlation (Fig. 6a). Figure 6b shows the symmetric component of the cross-correlation. Figure 6c is the positive component of the original cross-correlation, which is free from the Kyushu disturbance. In the frequency-time diagrams (e.g., Ritzwoller and Levshin, 1998), large differences between positive and negative correlation lag times are observed at periods shorter than 18 sec, especially in the group velocity dispersion curves. The Kyushu signal causes the measured group velocity to bias towards higher velocities (Fig. 6f). At periods longer than 18 sec, however, differences are quite small.

Therefore, to separate the Rayleigh wave from the Kyushu signal we must measure the Rayleigh wave dispersion on the correlation lag opposite from the arrival of the Kyushu signal in the period band of disturbance. The symmetric component, the average of the cross-correlation at positive and negative lag, cannot be used if the Kyushu signal arrives near the inter-station Rayleigh wave at either positive or negative correlation lag time.

In practice, we take the following steps. At periods greater than 18 sec, we can ignore the Kyushu disturbance and use the symmetric component for dispersion measurement. At periods less than or equal to 18 sec, the relative arrival time of the Kyushu signal and the surface wave signal at 12 sec period guides the measurement. If the apparent speed of the Kyushu signal is greater than 4.5 km/s and the length of the inter-station path is longer than three wavelengths, then the Kyushu signal is well enough separated from the surface wave that phase and group velocities can be measured on the symmetric component. If the apparent speed of the Kyushu signal is less than 4.5 km/s, then we make group and phase velocity measurements on the correlation lag opposite from the Kyushu signal.

As Figure 6a exemplifies, the correlation lag on the opposite side of the Kyushu signal may have a smaller amplitude than the lag containing the Kyushu signal and will have a significantly lower SNR than the symmetric component. Thus, this data processing procedure lowers the SNR for many inter-station cross-correlations between 8 and 16 sec period. Because observations are discarded if SNR < 15, this reduces the data set appreciably as Table 1 shows. We are still left with sufficient high quality measurements to perform tomography across much of the study region, however, at periods of 12 sec and above.

Figure 7 shows the effect of this data processing procedure compared to if the interference of the Kyushu signal were completely ignored. If not treated, the Kyushu signal would have vitiated our maps predominantly in South Korea, the southern Sea of Japan, and in the Kyushu region at 12 sec and 14 sec period. Artifacts would have been much stronger on the group velocity than the

phase velocity maps. By 18 sec period, however, even if left untreated, the Kyushu signal would have only weak effects on the estimated maps.

4. Rayleigh Wave Tomography

Surface wave tomography is applied to the selected dispersion measurements to produce Rayleigh wave group and phase speed maps on a 0.5 by 0.5 degree grid using the ray-theoretic method of Barmin et al. (2001). Being mostly determined over regional (non-teleseismic) inter-station paths, the dispersion measurements observed here will not be affected strongly by off-great circle effects (e.g., Lin et al., 2009) except for relatively long paths undergoing a continent-ocean transition. This will primarily affect paths from Japanese F-Net to Chinese stations. Finite frequency effects will also be weak in the period band of study (Lin et al., 2011). The tomographic method is based on minimizing a penalty functional composed of a linear combination of data misfit, model smoothness, and model amplitude. The choice of the damping parameters is based on the optimization of data misfit and the recovery of coherent model features. Due to a shortage of measurements, we are unable to produce reliable maps below 10 sec period and above about 45 sec period. The resulting Rayleigh wave dispersion maps, therefore, are constructed between 12 and 20 sec on a 2 sec period grid and thereafter on a 5 sec grid to 45 sec period.

During tomography, resolution is also estimated via the method described by Barmin et al. (2001) with modifications presented by Levshin et al. (2005). Resolution is defined as twice the standard deviation of a 2-D Gaussian fit to the resolution surface at each geographic node. Examples of resolution maps and associated path coverage are plotted in Figure 8 for the 16 sec and 35 sec period measurements. Resolution is estimated to be about 100 km across most of the region from northeast China, north China, the Yellow Sea and the Korean Peninsula to the Sea of Japan. Although seismic stations are absent within the Sea of Japan and there is only one station in the Korean Peninsula, the resolution remains about 100 km because of many crossing paths.

However, paths through these regions are relatively long (many longer than 1000 km) and undergo a continent-ocean transition at least once. This causes some reduction in the fidelity of the images due to off-great-circle propagation (e.g., Lin et al., 2009) that will not be reflected in the resolution maps shown in Figure 8. Resolution is about 200-400 km near the boundary of our studied area where station coverage is sparse. At long periods, the area with good path coverage shrinks and resolution reduces due to the decrease in the number of measurements (Table 1). Resolution is indicated on the tomography maps by presenting the 100 km resolution contour and by truncating the maps where resolution degrades to being worse than 400 km.

Histograms of data misfit using the dispersion maps at periods of 14 sec, 20 sec, 30 sec, and 40 sec are plotted in Figure 9 for phase and group velocity. Group travel time misfits are typically 2-3 times larger than phase travel time misfits because phase velocity measurements are more accurate (Bensen et al. 2007; Lin et al., 2008) and group velocity sensitive kernels have a larger amplitude. The range of standard deviations of the group travel time misfits is 3.97-4.87 sec and that of phase travel time is 0.95 - 1.45 sec. Phase travel time misfits of ~1 sec between 14 and 30 sec period are indicative of the quality of the data set, being similar to misfits that result from USArray data (e.g., Lin et al., 2008).

5. Results and Discussion

Group and phase velocity maps at periods of 14, 20, 30, and 40 sec are plotted in Figures 10 and 11. Only those areas where the spatial resolution is better than 400 km are shown. The 100 km spatial resolution contour is also plotted as a continuous white line. The maps are most reliable inside of this contour line. The high-resolution area encompasses most of Sino-Korean craton, the Sea of Japan and the Yellow Sea as well as about half of Japan, but varies somewhat with period. Resolution is worst at the longest periods, although the 100 km resolution contour encompasses most of the study region even at 40 sec period.

For comparison with the 14 sec maps, we also plot phase and group velocity maps at 12 sec period in Figure 12. This is a period of particularly strong influence by the Kyushu microseism and the data set is quite a bit smaller than at 14 sec period. In oceanic areas the 12 and 14 sec maps can be quite different because the deeper penetration of the 14 sec kernel yields a differential sensitivity to the oceanic crust and uppermost mantle.

At each period, the group velocity measurements are sensitive to shallower structures than the phase velocities. Phase velocity maps, therefore, generally should be compared with somewhat shorter period group velocity maps. Consistent with this expectation, comparison between Figures 10 and 11 reveals that the phase velocity map at 14 sec is similar to the group velocity map at 20 sec and the phase velocity map at 20 sec is quite like to the group velocity pattern at 30 sec. Because of the lower uncertainty in the phase velocity measurements, however, the phase velocity maps generally are more accurate than the maps of group velocity.

The dispersion maps are sensitive to quite different structures between short and long periods and between continental and oceanic regions even at the same period. The short period dispersion maps (12, 14 sec group and phase velocity) are primarily sensitive to upper crustal velocities in continental areas, which are dominated by the presence or lack of sediments. In regions with oceanic crust, sensitivity is predominantly to uppermost mantle structure. At intermediate periods (20 sec phase velocity, 20-40 sec group velocity), the maps are mostly sensitive to mid- to lower-crustal velocities beneath continents and continent-ocean crustal thickness variations. At long periods (30-40 sec phase velocity), the maps predominantly reflect crustal thickness variations on the continent and uppermost mantle conditions beneath oceans.

5.1 Rayleigh wave dispersion maps

At short periods (12 sec and 14 sec), the dispersion maps in Figures 10-12 exhibit low velocity anomalies where sediments are present (Bassin et al., 2000); e.g., the Songliao Basin (SLB),

Bohai Bay (BH), North China Platform (NC), the Yellow Sea (ESYS), and the Tsushima Basin (TB) in the southern Sea of Japan. Higher velocities are imaged in the mountains surrounding the basins; e.g, the Great Xing'an Range (GXAR), Lesser Xing'an Range (LXAR), the Changbai Mountains (CBM), the Yinshan Mountains (YSM), and the Taihang Mountains (THM), which is consistent with the presence of crystalline rocks near the surface. Weak positive anomalies are observed in the Korean Peninsula. The pattern of the high and low anomalies in South Korea at 14 sec is similar to the result of Cho et al. (2007) at shorter periods and similarly weak anomalies are observed from short periods to long periods.

The 12 and 14 sec maps in Figures 10-12 are mostly similar to one another with the prominent exception being the group velocity in the Sea of Japan (Figure 10a, 12a). Group velocity anomalies at 12 sec period in the Sea of Japan are dominantly low, while at 14 sec they are dominantly high. This dramatic velocity difference is due to the thin crust in the Sea of Japan, which is believed to be about 9km thick beneath the Japan Basin (JB) (Sato et al., 2004), 15km thick beneath the Tsushima Basin (TB) (Kim et al., 1994), but may extend as deep as 22km beneath the Yamamoto Rise (Kurashimo et al., 1996). Group velocities at 12 sec are affected mainly by oceanic crustal shear wave speeds whereas at 14 sec they are mostly sensitive to the upper mantle.

At intermediate periods (20 sec phase velocity, 20-30 sec group velocity), relatively low wave speeds are still observed for the deeper basins: Songliao, Bohai Bay, North China Platform and Yellow Sea. As at 14 sec period, group and phase velocity remain very high in the Sea of Japan reflecting oceanic mantle lithospheric shear wave speeds. A significant low velocity anomaly appears in Xingan-East Mongolia. The anomaly does not develop along the Tangcheng-Lujiang Fault, however, but rather to the west of the Songliao Basin, encompassing the Great Xing'an Range and the Yinshan Mountains north of the Ordos Block. To the east of the NSGL the crust is much thinner than to its west (e.g., Xu, 2007).

At intermediate periods, the phase and group velocity anomalies in the Sea of Japan are exceptionally high and clearly outline the continental boundary of the oceanic crust. It should be noted that off-great circle effects that may exist are not severe enough to distort the borders of the oceanic crust badly.

For phase velocity at periods of 30-40 sec and above, three principal observations are worth noting. First, the high wave speed anomalies of the Sea of Japan diminish from 30 sec to 40 sec period on the phase velocity maps. This is probably a reflection of the relatively young thin lithosphere beneath the Sea of Japan and increased sensitivity to the underlying asthenosphere by the longer period waves. The lower phase velocities of the southern Sea of Japan, in particular the Yamamoto Basin (YB) and the Tsushima Basin (TB), compared with more northern regions of the sea may also reflect the origin of the TB and the YB in stretched continental crust (Taira, 2001). Second, the Songliao and Bohai basins are situated within the Songliao-Bohai Graben, which is believed to have formed by back-arc extension and potential rifting (Liu et al., 2001). This graben, extending from the Songliao Basin into Bohai Bay, is associated with a continuous high velocity anomaly, which is clearly observable on the 30 and 40 sec phase velocity maps. In fact, this high velocity anomaly extends further, from Bohai Bay into the Yellow Sea. The Tangcheng-Lujiang Fault defines the eastern flank of the graben near the Songliao Basin, and clearly distinguishes low phase speeds of the Northeast Asia Foldbelt from the high wave speeds of the basin. The Great Xing'an Mountains define the western flank of the graben, and also mark the lower wave speeds that exist outside the graben. The high phase velocities in this period range for the Songliao-Bohai Graben are probably caused by thinner crust. The extension of the high velocity anomaly beneath the Yellow Sea may indicate continuation of a potential rift feature outside the known graben. Third, on the longest period phase velocity maps, low wave speeds are found along the entire length of the Northeast Asia Foldbelt, including the Korean Peninsula. Such clear continuous low wave speeds are not apparent on the 40 sec group velocity map because of the shallower sensitivity of group velocities than phase velocities. Apparent

discrepancies between phase and group velocities such as this one are reconcilable by inversion for a crustal and uppermost mantle Vs model, as shown in section 5.2.

Across all periods from 14 sec to 40 sec, low velocity anomalies are coincident with the Changbai volcanic area just north of the Korean Peninsula. In this area the phase velocity perturbation is typically about -3%, which is 1-2% lower than the surroundings. Because crustal thickness in this area is probably only ~35km (e.g., Shin and Baag, 2000), these anomalies may be due to elevated crustal and uppermost mantle temperatures, which would agree with results from receiver function studies (Hetland et al., 2004). The area of the low velocity anomalies extends eastward and widens with increasing period. Similar results are found with body wave tomography (Lei and Zhou, 2005), in which the Changbai volcano is shown to extend to about 400 km depth, the low wave speeds extend eastward with depth, and the width of the anomaly increases up to 200 km beneath 200 km depth.

Another noticable low velocity anomaly in the phase speed maps from 14 to 40 sec period is located at the Yinshan Mountains near the northeast corner of the Ordos block. The phase velocity perturbation is typically about -4% to-6%, which is 3%-5% lower than the surrounding areas. The spatial scale of this low velocity anomaly shrinks with depth: at short to medium periods (14~20 sec), the anomaly is composed of an E-W trend low velocity belt and a SW-NE trending low velocity zone, which is consistent with the Hetao rift to the north of the Ordos block and the Shanxi rift to the east of the Ordos block. At medium to long periods (30 ~ 40 sec), these two low velocity belts merge into a single low velocity anomaly, and shrink with increasing period. At the periods longer than 40 sec, only the cross point of these two velocity belts continues as a strong low velocity perturbation. This low velocity zone is consistent with the Quaternary Datong volcanic cluster in the Shanxi Province and the relatively younger Honggeertu volcano in Mongolia Province (Wei et al., 2003). Because the size of the low velocity zone shrinks with period quickly, and at short periods this low velocity anomaly

comprises by two velocity belts, we suggest that these volcanoes may not be deeply rooted, and the volcanoes are generated by the spreading of the Shanxi rift and the Hetao rift because of the counter clockwise rotation of the Ordos block (e.g. Zhang et al., 1998).

5.2 Dispersion curves and Vs structure at six locations

The production of a 3-D model of the entire region of study is beyond the scope of the present paper. However, to gain insight into the crustal and uppermost mantle structures responsible for the features presented in Figures 10-12 we present local dispersion curves (Fig. 13) and local Vs models (Fig. 14) determined from those curves for the eight locations identified in Figure 1a. These locations are: the Japan Basin in the Sea of Japan (A), the Songliao Basin (B), Honshu Island (C), the Korean Peninsula (D), the North China Platform (E), the Yellow Sea Basin (F), the Great Xing'an Range (G), and the Changbai volcanic zone (H). The group velocity and phase velocity curves shown in Figure 13 are mostly smoothly varying and are able to be fit by a vertically simple Vs model at each point within observational error. In particular, the group and phase velocity curves are reconcilable at each point. Misfit is presented for each point in Figure 13, where "RMS misfit" means the square root of the reduced chi-square value:

$$\text{RMS misfit} = \left[\frac{1}{N} \sum_i \frac{(d_i - p_i)^2}{\sigma_i^2} \right]^{\frac{1}{2}} \quad (1)$$

where d_i is the observed group or phase velocity value, p_i is the valued predicted from the model, σ_i is the uncertainty for the observation, and N is the total number of phase plus group velocity values along the dispersion curves.

Uncertainties in the phase velocity curves can be estimated by using the eikonal tomography method (Lin et al., 2009). This method, however, requires a more uniform array spacing than exists in the present study. Therefore, the uncertainties shown in Figure 13 are not formally for

the data set presented here. However, as discussed in section 2, misfit statistics in the present study are similar to those that emerge in the western US based on the regularly spaced USArray Transportable Array. For this reason, we apply these uncertainties here, but to be conservative we double average uncertainties estimate by eikonal tomography in the western US (Lin et al., 2009; Moschetti et al., 2010a, 2010b). The dispersion curves at the chosen locations are quite different from one another.

To produce the vertical V_s profiles at each point we perform a Monte-Carlo inversion similar to that performed by Shapiro and Ritzwoller (2002) and Moschetti et al. (2010b). At each location a corridor of V_s models emerges which represents 2σ variations in V_s and 1σ variations across the two model discontinuities that occur at the base of the sediments and at Moho. The model parameterization differs from Moschetti et al. (2010b) only in that smooth basis functions are used in the crust (rather than a stack of constant velocity layers) and Love waves are not inverted. Thus, the model is actually a V_{sv} model.

Differences exist between the eight vertical V_s profiles in the thickness of the sedimentary layer, crustal thickness, and the shear wave velocities in the crust and uppermost mantle. Some of these characteristics are summarized in Table 2. Uncertainties in these estimates largely reflect trade-offs between the model parameters.

Non-negligible sediments are found only in the Sea of Japan (Fig. 14a), the North China Platform (Fig. 14e) and particularly in the Songliao Basin (Fig. 14b). Sediment layer thickness in the Songliao Basin is estimated to be ~3±1.5 km with velocities ranging from 1.2 km/s to 3 km/s. Surface waves do not constrain sedimentary structures well, but it is important to specify sediments in the inversion in order not to bias underlying crystalline crustal values.

Crustal thickness varies appreciably between the different locations. Not surprisingly, the thinnest crust is found beneath the Sea of Japan being approximately 16±4 km, which is in agreement with prior studies (e.g., Kim et al., 1994). The thickest crust in the region is found

beneath the Great Xing'an Range and the Changbai Volcano, ranging between 37 and 40 km with uncertainties between 4 and 7 km. The crust beneath the Korean Peninsula is estimated to be somewhat thinner, 30±5 km. The large uncertainties in these values reflect the difficulty to estimate crustal thickness with surface waves. Distinctly thinner continental crust is found beneath the Songliao Basin (27±3 km) and the Yellow Sea (33±3 km). The crust of the North China Platform is also thin, being 32±4km, which is much thinner than the Ordos block (e.g., Zheng et al., 2010b).

At 20 km depth, shear wave speeds are highest beneath the Sea of Japan (4.3±0.12 km/s) because this is a oceanic mantle depth. At 20 km depth at the seven continental locations, shear wave speeds are similar, ranging from 3.53 to 3.63 km/s with uncertainties of 40 - 80 m/s. The Korean Peninsula has a clearly faster shear wave speed at 20 km depth than the other continental locations, being 3.67±0.05 km/s, consistent with it being a stable cratonic remnant.

The lowst velocities at 80 km depth are beneath the Changbai Volcano (4.21±0.07km/s) and the Sea of Japan (~4.32±0.08 km/s), probably indicating localized heating beneath the volcano and thin lithosphere beneath this oceanic point. The fastest mantle velocities are beneath the Great Xing-an Range, the Songliao Basin, and the Yellow Sea, all being about 4.43±0.08 km/s. The mantle beneath the Korean Peninsula is intermediate between these other points.

7. Conclusions

This paper represents a major step toward a high resolution 3-D shear velocity model of the crust and uppermost mantle across northeastern China, the Sea of Japan, and the Korean Peninsula by presenting a study of the dispersion characteristics of Rayleigh waves obtained from ambient noise cross-correlations. Broadband stations from Chinese Provincial Networks, the Japanese F-Net, and the IRIS GSN have produced two-year continuous time series from 2007 into 2009 that form the basis for these results. Phase and group velocity maps from 12 sec to 45 sec period are constructed, which constrain earth structures in the crust and uppermost mantle to a depth of

about 80 km. The dispersion maps are geologically coherent, displaying the signatures of sedimentary basins, mountain roots, ocean-continent variations, and anomalies due to rifting and volcanism. The maps at different periods and between phase and group velocities are consistent with one another, and vertically relatively smooth Vs models fit the observations.

To generate the dispersion maps presented here, the effects of the persistent localized Kyushsu microseism had to be eliminated in the dispersion measurements. We present a method based on locating the microseism (thereby confirming the location of Zeng and Ni, 2010), predicting the arrival of the disturbing signal on the ambient noise cross-correlations, and obtaining the dispersion measurements at opposite cross-correlation lag times from the Kyushu signal.

The principal observations, therefore, are in place to produce a 3-D model of the crust and uppermost mantle to a depth of about 80 km. Such a model is motivated to produce new constraints on the massive volcanism, crustal extension, cratonic rejuvenation, and lithospheric thinning that are hypothesized for northeastern China. Ambient noise tomography is particularly needed to constrain the structure of the crust, and complements information from body wave travel times, receiver functions, longer period teleseismic surface waves, gravity, and other types of data. Assimilating similar results from a companion paper for southeastern China (Zhou et al., 2011), will allow the 3-D model to extend across all of eastern China.

In addition to the production of a 3-D Vs model of the crust and uppermost mantle, other research envisioned that may be derived from this work includes the estimation of azimuthal anisotropy, which will place complementary constraints on the physical processes that motive this study. In addition, future understanding of the dispersion characteristics of Love waves will allow estimation of radial anisotropy that reflects deformation undergone by the crust and uppermost mantle. The geometry of the observing array makes the application of differential travel time methods for earthquakes difficult, such as eikonal tomography (Lin et al., 2009), Helmholtz tomography (Lin and Ritzwoller, 2011), or two-plane wave tomography (e.g., Yang et

al., 2008b). However, the success of such methods would allow dispersion maps to be extended to longer periods and, hence, to produce better constraints on the structure of the mantle.

Acknowledgement. The authors thank Fan-Chi Lin for valuable conversations. This work was supported by CAS grant kzcx2-yw-142, NSFC grant 40974034, grant 201008007 from CEA, US NSF-EAR award 0944022, and US NSF-OISE sub-award 0730154. Most of the waveform data for this study were provided by the Data Management Centre of the China National Seismic Network at the Institute of Geophysics, China Earthquake Administration and F-Net in Japan. In addition, the facilities of the IRIS Data Management System were used to access data required in this study. The IRIS DMS is funded through the US National Science Foundation under Cooperative Agreement EAR-0552316.

References

Bai, L., H. Kawakatsu, and Y. Morita (2010), Two anisotropic layers in central orogenic belt of the North China Craton, Tectonophysics, 494, 138-148.

Barmin, M. P., M. H. Ritzwoller, and A. L. Levshin (2001), A fast and reliable method for surface wave tomography, *Pure Appl. Geophs.*, 158:1351-1375.

Bassin, C., G. Laske, and G. Masters (2000), The current limits of resolution for surface wave tomography in North America. *EOS Trans AGU 81,* F897.

Bensen, G. D., M. H. Ritzwoller, M. P. Barmin, A. L. Levshin, F. Lin, M. P. Moschetti, N. M. Shapiro, and Y. Yang (2007), Processing seismic ambient noise data to obtain reliable broad-band surface wave dispersion measurements, *Geophys. J. Int.*, 169: 1239-1260.

Bensen, G.D., M.H. Ritzwoller, and N.M. Shapiro (2008), Broad-band ambient noise surface wave tomography across the United States, *J. Geophys. Res.*, 113, B05306, 21 pages, doi:10.1029/2007JB005248, 2008.

Bensen, G. D., M. H. Ritzwoller and Y. Yang (2009), A 3-D shear velocity model of the crust and uppermost mantle beneath the United States from ambient seismic noise. *Geophys. J. Int.*, 177: 1177-1196.

Bourova, E., K. Yoshizawa, and K. Yomogida (2010). Upper mantle structure of marginal seas and subduction zones in northeastern Eurasia from Rayleigh wave tomography, *Phys. Earth. Planet. Int.*, 183:20-32.

Chen, L., C. Cheng, and Z. Wei (2009), Seismic evidence for significant lateral variations in lithospheric thickness beneath the central and western North China Craton, *Earth Planet. Sci. Lett.,* 286, 171-183.

Cho, K.H., Herrmann, R.B., Ammon, C.J., Lee, K. (2007), Imaging the upper crust of the Korean Peninsula by surface-wave tomography. *Bull. Seism. Soc. Am.,* **97** (1), 198-207 Part B Sp. Iss. S.

Deng, J., S. Su, Y. Niu, C. Liu. G. Zhao, X. Zhao, S. Zhou, and Z. Wu (2007), A possible model for the lithospheric thinning of the North China Craton: Evidence from the Yanshanian (Jura-Cretaceous) magmatism and tectonism, Lithos, 96, 22-35.

Gao, S. R.L. Rudnick, H. -L. Yuan, X. –M. Liu, Y. –S. Liu, W. –L. Xu, W. –L. Ling, J. Ayers, X. –C. Wang, and Q. –H. Wang (2004), Recycling lower continental crust in the North China craton, *Nature*, 432, 892-897.

Gao, S. R.L. Rudnick, W.-L. Xu, H.-L. Yuan, Y-S. Liu, R. J. Walker, I.S. Puchtel, X. Liu, H. Huang, X.-R. Wang, J. Yang (2008), Recycling deep cratonic lithosphere and generation of intraplate magmatism in the North China Craton, *Earth Planet. Science Lett.,* 270, 41-53.

Griffin, W.L., A. Zhang, S.Y. O'Reilly, C.G. Ryan (1998), Phanerozoic evolution of the lithosphere beneath the Sino-Korean Craton. In: Flower, M.J., S.-L. Chung, C.-H. Lo, T-Y. Lee (Eds.), Mantle dynamics and plate interactions in East Asia, AGU Geodynamics Series, Vol. 27, 107-126.

Guo, Z., X. Gao, H. Yao, J. Li, W. Wang (2009), Mid-crustal low velocity layer beneath the central Himalaya and southern Tibet revealed by ambient noise array tomography, *Geochem. Geophys. Geosyst.,* 10(5), Q05007, doi:10.1029/2009GC002458.

Fang, L., J. Wu, Z. Ding, G.F. Panza (2010), High resolution Rayleigh wave group velocity tomography in North China from ambient noise, *Geophys. J. Int.*, 181, 1171-1182.

He, Z.Q., T.L. Ye, and Z.F. Ding (2009), Surface wave tomography for the phase velocity in the northeastern part of North China, *Chinese J. Geophys.*, 52(5), 1233-1242.

Hetland, E.A., F.T. Wu, J.L. Song (2004), Crustal structure in the Changbaishan volcanic area, China, determined by modeling receiver functions. *Tectonophysics,* 386: 157-175.

Huang, H., H. Yao, and R.D. van der Hilst (2010), Radial anisotropy in the crust of SE Tibet and SW China from ambient noise interferometry, *Geophys. Res. Lett.,* 37, L21310, 5 pp., doi:10.1029/2010GL044981.

Huang, J. and D. Zhao (2006), High-resolution mantle tomography of China and surrounding regions, *J. Geophys. Res.*, 111, doi:10.1029/2005JB004066.

Huang, Z., H. Li, Y. Zheng, and Y. Peng (2009), The lithosphere of North China Craton from surface wave

tomography, *Earth Planet. Sci. Lett.,* 288, 164-173.

Huang, Z., Y. Peng, Y. Luo, Y. Zheng, W. Su (2004), Azimuthal anisotropy of Rayleigh waves in East Asia. *Geophys. Res. Lett.* 31, L15617. doi:10.1029/2004GL020399.

Huang, Z. X., W. Su, Y. J. Peng, Y. J. Zheng, and H. Y. Li (2003), Rayleigh wave tomography of China and adjacent regions, *J. Geophys. Res.*, 108, doi:10.1029/2001JB001696.

Jolivet, L. K., K. Tamaki, M. Fournier (1994), Japan Sea, opening history and mechanism: a synthesis. *J. Geophys. Res.* 99:22237-22259.

Kang, T.S. and Shin, J.S. (2006), Surface-wave tomography from ambient seismic noise of accelerograph networks in southern Korea. *Geophys. Res. Lett.* **33** (17), L17303.

Kim, H.J., C.H. Park, J.K. Hong, H.T. Jou, T.W. Chung, V. Zhigulef, G.I. Anosov (1994), Seismic experiment in the Ulleung Basin (Tsushima Basin), southwestern Japan Sea (East Sea of Korea). *Geophys. Res. Lett.* 21: 1975-1978.

Kurashimo, E., Shinohara, M., Suyehiro, K., Kasahara, J., Hirata, N. (1996), Seismic evidence for stretched continental crust in the Japan Sea. Geophys. Res. Lett. 23, 3067-3070.

Lei, J. and Zhao, D. (2005), P-wave tomography and origin of the Changbai intraplate volcano in Northeast Asia. *Tectonophysics*, 397, 281–295.

Lebedev, S., and G. Nolet (2003), Upper mantle beneath Southeast Asia from S velocity tomography, *J. Geophys. Res.*, 108, doi:10.1029/2000JB000073.

Levshin, A.L., M.H. Ritzwoller, and J.S. Resovsky (1999), Source effects on surface wave group travel times and group velocity maps, *Phys. Earth Planet. Int.*, 115, 293 - 312.

Levshin, A.L., M.P. Barmin, M.H. Ritzwoller, and J. Trampert (2005), Minor-arc and major-arc global surface wave diffraction tomography, *Phys. Earth Planet. Ints.*, 149, 205-223.

Li, C. and R.D. van der Hilst (2010), Structure of the upper mantle and transition zone beneath Southeast Asia from traveltime tomography, J. Geophys. Res., 115, B07308, doi:1029/2009JB006882.

Li, H.Y., W. Su, , C.Y.Wang, , Z. X. Huang (2009), Ambient noise Rayleigh wave tomography in western Sichuan and eastern Tibet. *Earth Planet. Sci. Lett.* 282 (1-4): 201-211.

Li, J. and F. Niu (2010), Seismic anisotropy and mantle flow beneath northeast China inferred from regional seismic networks, *J. Geophys. Res.*, 115, B12327, doi:10.1029/2010JB007470.

Li, Z., Hao T.Y., and Y. Xu (2011), Uppermost mantle structure of the North China Craton: Constraints from interstation Pn travel time diference tomography, *Chin. Sci. Bull.,* 56, 1691-1699.

Lin, F.C., M.P. Moschetti, and M.H. Ritzwoller (2008), Surface wave tomography of the western United States

from ambient seismic noise: Rayleigh and Love wave phase velocity maps, *Geophys. J. Int.*, doi:10.1111/j1365-246X.2008.03720.x.

Lin, F.C. and M.H. Ritzwoller (2011), Helmholtz surface wave tomography for isotropic and azimuthally anisotropic structure, *Geophys. J. Int.*, in press.

Lin, F.C., M.H. Ritzwoller, and R. Snieder (2009), Eikonal tomography: Surface wave tomography by phase-front tracking across a regional broad-band seismic array, *Geophys. J. Int.*, 177(3), 1091-1110.

Lin, F.C., M.H. Ritzwoller, Y. Yang, M.P. Moschetti, and M.J. Fouch (2011), Complex and variable crustal and uppermost mantle seismic anisotropy in the western United States , *Nature Geoscience*, Vol 4, Issue 1, 55-61.

Liu, J. J. Han, and W.S. Fyfe (2001), Cenozoic episodic volcanism and continental rifting in Northeast China and possible link to Japan Sea development as revealed from K-Ar geochronology, *Tectonophysics*, 339, 385-401.

Menzies, M.A.,W. Fan, and M. Zhang (1993), Paleozoic and Cenozoic lithoprobes and the loss of >120 km of Archean lithosphere, Sino-Korean craton, *China. Geol. Soc. Long. Spec. Pub.*, 76, 71-81.

Menzies, M., Y. Xu, H. Zhang, and W. Fan (2007), An integration of geology, geophysics, and geochemistry: A key to understanding the North China Craton, *Lithos*, 96, 1-21.

Moschetti, M.P., M.H. Ritzwoller, and F.C. Lin (2010a), Seismic evidence for widespread crustal deformation caused by extension in the western USA, *Nature*, 464, Number 7290, 885-889, 8 April 2010.

Moschetti, M.P., M.H. Ritzwoller, F.C. Lin, and Y. Yang (2010b), Crustal shear velocity structure of the western US inferred from ambient noise and earthquake data, *J. Geophys. Res.*, 115, B10306, doi:10.1029/2010JB007448.

Moschetti, M., M. Ritzwoller, and N. Shapiro (2007), Surface wave tomography of the western United States from ambient seismic noise: Rayleigh wave group velocity maps, *Geochem. Geophys. Geosyst.*, 8, Q08010, doi:10.1029/2007GC001655.

Nishida, K., Kawakatsu, H., Obara, K. (2008), Three-dimensional crustal S wave velocity structure in Japan using microseismic data recorded by Hi-net tiltmeters. *J. Geophys. Res.-Solid Earth,* **113** (B10), B10302.

Okada, Y., K. Kasahara, S. Hori, K. Obara, S. Sekiguchi, H. Fujiwara, and A. Yamamoto (2004), Recent progress of seismic observation networks in Japan – Hi-net, F-net, K-Net and KiK-net, *Earth Planets Space*, 56, xv-xxviii.

Pan, J.T., Q.J. Wu, Y.H. Li, F.X. Zhang, G.C. Zhang (2011), Rayleigh wave tomography of the phase velocity in North China, *Chinese J. Geophys.*, 54(1), 67-76.

Priestley, K., Debayle, E., McKenzie, D., Pilidou, S. (2006), Upper mantle structure of eastern Asia from

multimode surface waveform tomography. *J. Geophys. Res.* 111, B10304. doi:10.1029/2005JB004082.

Ren, J. K. Tamaki, S. Li, and J. Zhang (2002). Late Mesozoic and Cenozoic rifting and its dynamic setting in eastern China and adjacent seas, *Tectonophysics*, 344, 175-205.

Richard, G.C. and H. Iwamori (2010), Stagnant slab, wet plumes, and Cenozoic volcanism in East Asia, *Phys. Earth Planet. Int.*, 183, 280-287.

Ritzwoller, M.H. and A.L. Levshin (1998), Eurasian surface wave tomography: Group velocities, *J. Geophys. Res.*, 103, 4839 - 4878.

Ritzwoller, M.H., A.L. Levshin, L.I. Ratnikova, and A.A. Egorkin (1998), Intermediate period group velocity maps across Central Asia, Western China, and parts of the Middle East, *Geophys. J. Int.*, 134, 315-328.

Rogers, J.J.W. and M. Santosh (2006), The Sino-Korean Craton and supercontinent history: Problems and perspectives, *Gondwana Res.,* 9, 21-23.

Sabra, K. G., P. Gerstoft, P. Roux, W. A. Kuperman, and M. C. Fehler (2005), Surface wave tomography from microseisms in Southern California, *Geophys. Res. Lett.* 32, L14311.

Santosh, M., D. Zhao, and T. Kusky (2010), Mantle dynamics of the Paleoproterozoic North China Craton: A perspective based on seismic tomography, *J. Geodyn.* 49, 39-53.

Sato, T., Shinohara, M., Karp, B.Y., Kulinich, R.G., Isezaki, N. (2004), P-wave velocity structure in the northern part of the central Japan Basin, Japan Sea with ocean bottom seismometers and airguns. *Earth Planets Space,* 56: 501–510.

Shapiro, N.M. and M.H. Ritzwoller (2002), Monte-Carlo inversion for a global shear velocity model of the crust and upper mantle, *Geophys. J. Int.*, 151, 88-105.

Shapiro, N. M., M. Campillo, L. Stehly, and M. H. Ritzwoller (2005), High-resolution surface wave tomography from ambient seismic noise. *Science* 307, 1615-1618.

Shapiro, N.M., M.H. Ritzwoller, and G.D. Bensen (2006), Source location of the 26 sec microseism from cross correlations of ambient seismic noise, *Geophys. Res. Lett.*, 33, L18310, doi:10.1029/2006GL027010.

Shin, J.S. and C.E Baag (2000), Moho depths in the border region between northern Korea and northeastern China from waveform analysis of teleseismic pMP and pP phases. *Geosci. J.* (Seoul) 4: 313– 320.

Sun, Y. and N. Toksoz (2006), Crustal structure of China and surrounding regions from P wave travetime tomography, *J. Geophys. Res.,* 111, B03310, doi:10.1029/2005JB003962.

Sun, X., X. Song, S. Zheng, Y. Yang, M. Ritzwoller (2010), Three dimensional shear velocity structure of crust and upper mantle in China from ambient noise surface wave tomography, *Earthquake Science*, 23, 449-463, doi:10.1007/s11589-010-0744-3.

Taira, A. (2001), Tectonic evolution of the Japanese island arc system. *Annu. Rev. Earth Planet. Sci*, 29:109-134.

Tang, Q. and Chen, L. (2008), Structure of the crust and uppermost mantle of the Yanshan Belt and adjacent regions at the northeastern boundary of the North China Craton from Rayleigh wave dispersion analysis. *Tectonophysics* 455, 43–52.

Tatsumi, Y., Y. Otofuji, T. Matsuda, and S. Nohda (1989), Opening of the Sea of Japan back-arc basin by asthenospheric injection, *Tectonophysics*, 166, 317-329.

Tian, A.Y., P. Han, and K.D. Xu (1992), The Mesozoic-Cenozoic east China rift system, *Tectonophysics*, 208, 341-363.

Tian, Y., Zhao, D., Sun, R., Teng, J. (2009), Seismic imaging of the crust and upper mantle beneath the North China Craton, *Phys. Earth Planet. Int.*, 172, 169–182.

Villaseñor, A., Y. Yang, M. H. Ritzwoller, and J. Gallart (2007), Ambient noise surface wave tomography of the Iberian Peninsula: Implications for shallow seismic structure, *Geophys. Res. Lett.*, 34, L11304, doi:10.1029/2007GL030164.

Wei, H., R.S.J. Sparks, R. Liu, Q. Fan, Y. Wang, H. Hong, H. Zhang, H. Chen. C. Jiang, J. Dong, Y. Zheng, Y. Pan (2003), Three active volcanes in China and their hazards, *Journal of Asian Earth Sciences*, 21, 515-526.

Xu, P. and D. Zhao (2009), Upper-mantle velocity structure beneath the North China Craton: implications for lithospheric thinning, *Geophys. J. Int.*, 177, 1279-1283.

Xu, Y. G. (2007), Diachronous lithospheric thinning of the North China Craton and formation of the Daxin'anling-Taihangshan gravity lineament, *Lithos*, 96, 281-298.

Yang, Y., M. Ritzwoller. A. Levshin, and N. Shapiro (2007), Ambient noise Rayleigh wave tomography across Europe. *Geophys. J. Int.*, 168: 259-274.

Yang, Y., and M. Ritzwoller (2008). Characteristics of ambient seismic noise as a source for surface wave tomography. *Geochem. Geophys. Geosyst.*, 9, Q02008, doi:10.1029/2007GC001814.

Yang, Y., A. Li, and M. Ritzwoller (2008a). Crustal and uppermost mantle structure in southern Africa revealed from ambient noise and teleseismic tomography. *Geophysi. J. Int.,* 174: 235-248.

Yang, Y., M. Ritzwoller, F.. Lin, M. Moschetti, and N. Shapiro (2008b), Structure of the crust and uppermost mantle beneath the western United States revealed by ambient noise and earthquake tomography, *J. Geophys. Res.*, 113, B12310, doi:10.1029/2008JB005833.

Yang, Y., Y. Zheng, J. Chen, S. Shou, S. Celyan, E. Sandvol, F. Rilmann, K. Priestley, T.M. Hearn, J.F. Ni, L.D. Brown, and M.H. Ritzwoller (2010), Rayleigh wave phase velocity maps of Tibet and the surrounding

regions from ambient seismic noise tomography, *Geochem., Geophys., Geosys.*, 11(8), Q08010, doi:10.1029/2010GC003119.

Yanovskaya, T.B., Kozhevnikov, V.M. (2003). 3D S-wave velocity pattern in the upper mantle beneath the continent of Asia from Rayleigh wave data. *Phys. Earth Planet. Int.* 138, 263–278.

Yao, H., R. D. van der Hilst, and M. V. de Hoop (2006), Surface-wave array tomography in SE Tibet from ambient seismic noise and two-station analysis—I. Phase velocity maps, *Geophys. J. Int.,* 166, 732–744, doi:10.1111/j.1365-246X.2006.03028.x.

Yao, H., C. Beghein, and R. D. van der Hilst (2008), Surface wave array tomography in SE Tibet from ambient seismic noise and two-station analysis—II. Crustal and upper-mantle structure, *Geophys. J. Int.*, 173, 205–219, doi:10.1111/j.1365-246X.2007.03696.x.

Yin, A. (2010), Cenozoic tectonic evolution of Asia: A preliminary synthesis, *Tectonophysics*, 488, 293-325.

Yoshizawa, K., K. Miyake, and K. Yomogida (2010), 3D upper mantle structure beneath Japan and its surrounding region from inter-station measurements of surface waves, *Phys. Earth Planet. Int.,* 183, 4-19.

Zeng, X, and S. Ni (2010), A persistent localized microseismic source near the Kyushu Island, Japan, *Geophys. Res. Lett.*, 37, L24307, doi:10.1029/2010GL045774.

Zhai, M., W. Fan, H. Zhang, J. Sui, and J. Shao (2007), Lower crustal processes leading to Mesozoic lithospheric thinning beneath eastern North China: Underplating, replacement, and delamination, Lithos, 96, 36-54.

Zhang, Y. Q., J. L. Mercier, P. Vergély (1998), Extension in the graben systems around the Ordos (China), and its contribution to the extension tectonics of south China with respect to Gobi-Mongolia, *Tectonophysics*, 285, 41-75.

Zhang, Z. M., J. G. Liou, and R. G. Coleman (1984), An outline of the plate tectonics of China, *Geol. Soc. Am. Bull*, 95, 295-312.

Zhao, D. (2009), Multiscale seismic tomography and mantle dynamics. *Gondwana Research*, 15, 297–323.

Zhao, L. T. Zheng, and G. Lu (2008), Insight into craton evolution: Constraints from shear wave splitting in the North China Craton, *Phys. Earth Planet. Int.,* 168, 153-162.

Zheng, S., X. Sun, X. Song, Y. Yang, and M.H. Ritzwoller (2008), Surface wave tomography of China from ambient seismic noise, *Geochem. Geophys. Geosyst.*, 9, Q0502, doi:10.1029/2008GC001981.

Zheng, T., L. Chen, L. Zhao, W. Xu, and R. Zhu (2006), Crust–mantle structure difference across the gravity gradient zone in North China Craton: Seismic image of the thinned continental crust, *Phys. Earth Planet. Int.,* 159, 43-58.

Zheng, X. F., Z. X. Yao, J. H. Liang, and J. Zheng (2010a), The role played and opportunities provided by IGP

DMC of China National Seismic Network in Wenchuan earthquake disaster relief and researches, *Bull. Seismol. Soc. Am.*, 100(5B), 2866-2872.

Zheng, Y., Y. Yang, M.H. Ritzwoller, X. Zheng, X. Xiong, Z. Li (2010b), Crustal structure of the northeastern Tibetan Plateau, the Ordos Block, and the Sichuan Basin from ambient noise tomography, *Earthquake Science*, 3, 465-476, doi:10.1007/s11589-010-0745-3.

Zhou, L. Q., Y. Zheng, W. S. Shen, Y. J. Yang, H. Shi, and M.H. Ritzwoller (2011), Ambient noise surface wave tomography of South China, submitted.

Zhou, R.M., B.W. Stump, R.B. Herrmann, Z. X. Yang, and Y. T. Chen (2009), Teleseismic receiver function and surface-wave study of velocity structure beneath the Yanqing-Huailai Basin Northwest of Beijing, *Bull. Seism. Soc. Am.*, 99(3), 1937-1952.

Table 1: Number of measurements retained after each step in data quality control.

Period (s)	Step A	Step B	Step C	Step D	Step E (phase)	Step E (group)
12	27033	20732	20701	19365	17887	16873
14	31356	25770	25740	24082	22606	21593
20	33573	33573	33564	31555	29835	30250
25	28990	28990	28982	27398	25561	25878
30	25495	25495	25491	24210	22258	22148
35	21976	21976	21972	20985	18991	18663
40	18172	18172	18165	17488	15432	14984
45	14503	14503	14495	14031	11991	11575

Table 2. Characteristics of the ensemble of V_s models at eight locations (Fig. 2): A. Sea of Japan, B. Songliao Basin, C. Honshu, D. Korean Peninsula, E. North China Platform, F. Yellow Sea, G. Great Xing'an Range, and H. Changbai volcano.

	A	B	C	D	E	F	G	H
Thickness(km), sediments	1.04± 0.44	3.24± 1.47	0.26± 0.14	0.23± 0.12	3.21± 1.34	0.77± 0.52	0.23± 0.12	0.21± 0.12
Thickness (km), crust	16.4± 4.2	26.9± 3.2	29.8± 4.4	30.2± 4.6	31.9± 4.2	32.8± 3.2	37.2± 4.1	40.0± 7.2
Vsv (km/s), 20km	4.34± 0.13	3.53± 0.08	3.51± 0.05	3.63± 0.05	3.59± 0.08	3.59± 0.05	3.59± 0.04	3.59± 0.05
Vsv (km/s), 80km	4.32± 0.08	4.45± 0.07	4.28± 0.05	4.26± 0.07	4.41± 0.07	4.43± 0.06	4.43± 0.08	4.21± 0.07

Figures and Captions

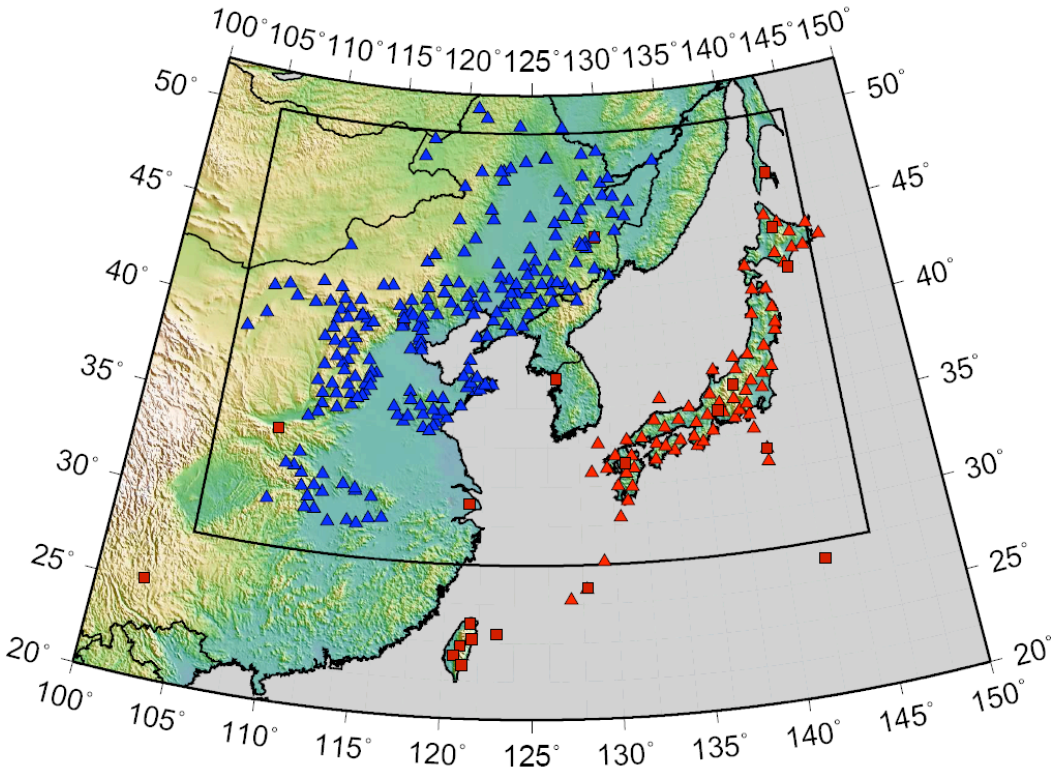

Figure 1. The broadband seismic stations used in this study. The blue triangles are the Chinese provincial broadband seismic stations, the red triangles are the F-Net long period stations and the red squares are other broadband stations, mostly from the IRIS GSN. The rectangle outlined by the black lines defines the study region.

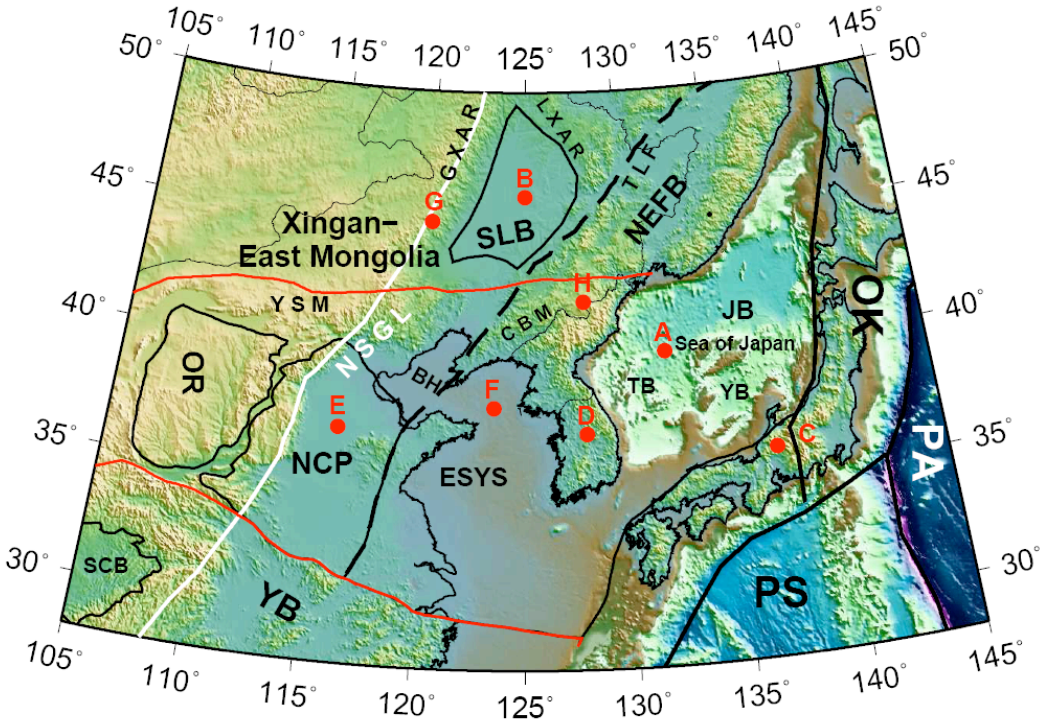

Figure 2. The tectonics setting of this study. Red lines mark the boundaries of the Sino-Korean Craton (SKC), the solid white line identifies the North South Gravity Lineament (NSGL), the dashed white line is the Tancheng-Lujiang fault (TLF), and black lines outline the blocks and tectonic boundaries (Zhang, et al., 2003). Tectonic feature names are abbreviated as follows: PA: Pacific Plate, PS: Phillipine Sea Plate, OK; Okhotsk Plate, NCP: North China Platform, YB: Yangtze Block, SLB: Songliao Basin, JB: Japan Basin; TB: Yamato Basin, TB: Tsushima Basin, SB: Sichuan Basin, OR: Ordos Block, BH: Bohai Bay, GXAR: Great Xing'an Range, LXAR: Lesser Xing'an Range, CBM: Changbai Mountain Range, YSM: Yinshan Mountain Range, ESYS: East Shandong Yellow Sea Block, NEFB: Northeast Asian Fold Belt. Red dots mark locations of the dispersion curves and 1D shear velocity profiles in eight tectonic units. A: the Sea of Japan, B: the Songliao Basin, C: Honshu, D: Korean Peninsula, E: North China Platform, F: the Yellow Sea Basin, G: the Great Xing'an Range, and H: Changbai Volcano.

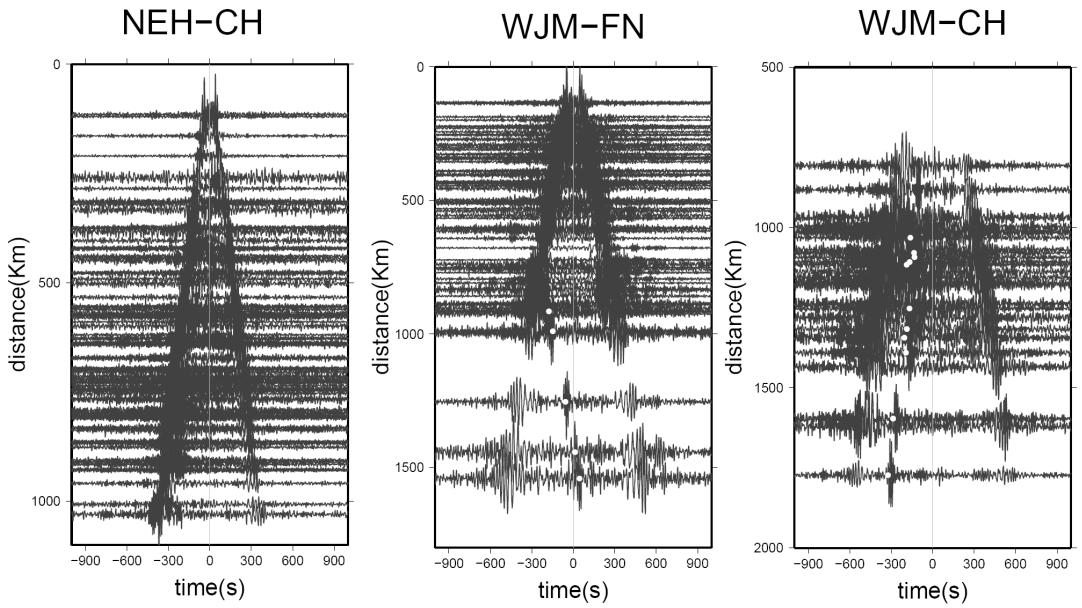

Figure 3. Record sections of cross-correlations obtained from two years of waveform data (a) between Chinese provincial network stations, (b) between F-Net stations, and (c) between the Chinese stations and F-Net stations. The white dots identify the expected arrival times for the Kyushu persistent microseism.

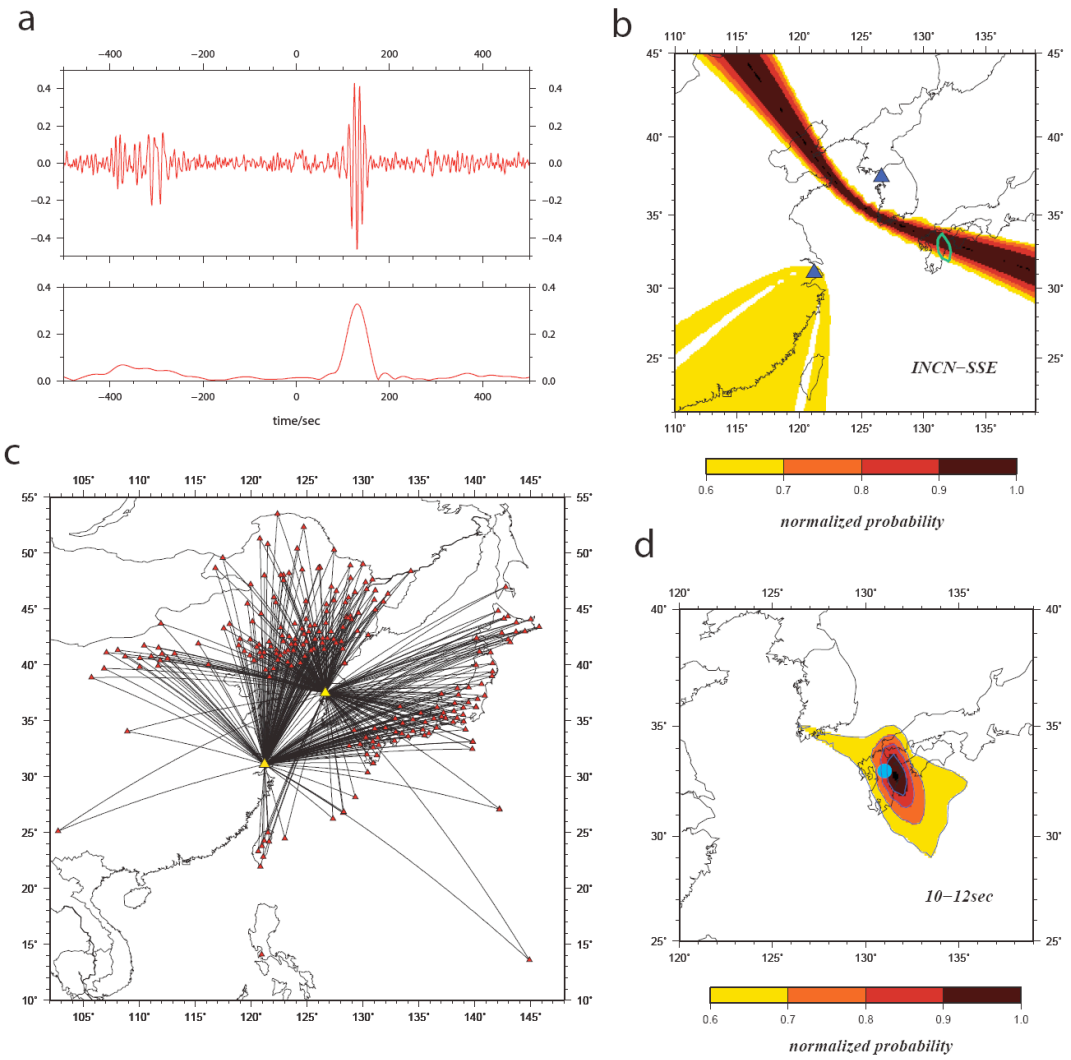

Figure 4. (a) Top Panel: raw cross-correlation (CC) between station SSE and INCN (blue triangles in (b). Bottom Panel: The envelope function of the CC filtered between 8 and 10 sec period. The Kyushu microseismic signal arrives at ~130 sec. (b) The migrated hyperbola from the envelope function in (a). The map is normalized so its maximum value is 1. The green contour is the 0.9 isoline from (d). (c) Paths used to locate the Kyushu micro-seismic signal are plotted with black lines. We use all paths associated with station SSE and INCN (yellow triangles). (d) Stack of migrated hyperbolas to locate the Kyushu microseism. Blue circle is the location previously determined by Zeng and Ni (2010).

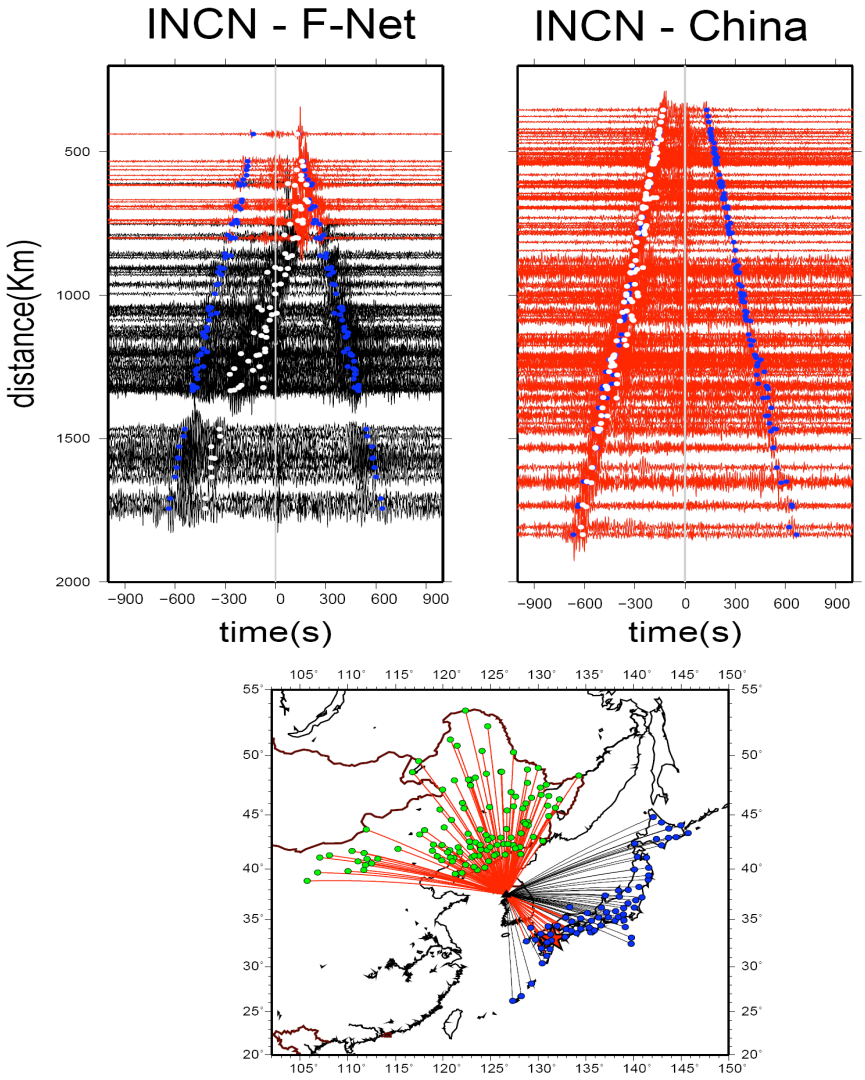

Figure 5. Examples of cross-correlations disturbed by the Kyushu persistent microseism. (a) Record section for station INCN (GSN, South Korea) and F-Net stations. White dots are the expected travel times of the persistent Kyushu microseism, blue dots are approximate theoretical arrival times of the ambient noise empirical Green's functions, and red traces identify the disturbed waveforms (i.e., group velocity of the Kyushu signal is less than 4.5 km/s). (b) Record sections between station INCN and China seismic stations where the trace and dot colors are as in (a). (c) For the traces in (a) and (b) the green and blue dots are the Chinese provincial and F-Net stations, respectively. The red star is the general location of the Kyushu signal. Red traces are the paths disturbed by the Kyushu signal, while the black lines are undisturbed paths.

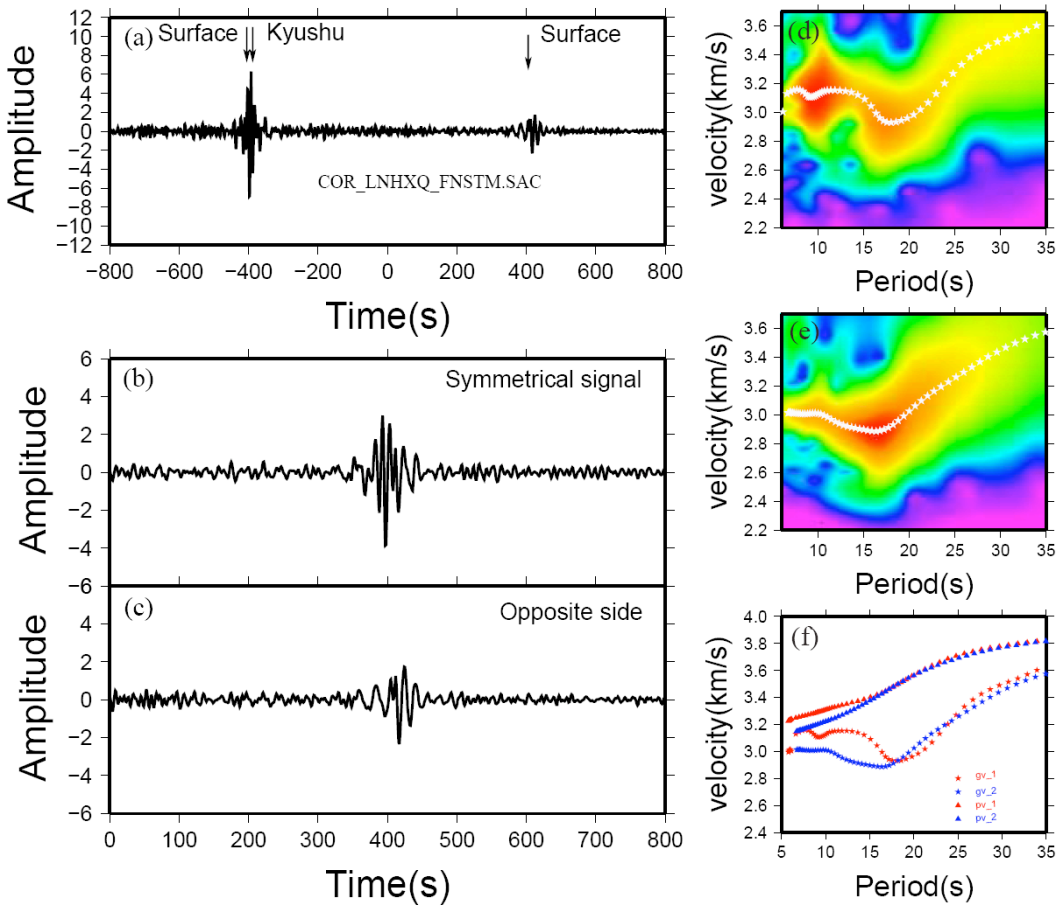

Figure 6. Cross-correlations and corresponding frequency-time diagrams illustrating the effect of the persistent Kyushu microseism. (a) Cross-correlation between stations HXQ of the Chinese network and STM of F-Net, where the expected arrival time of the signal from the Kyushu microseism is close to the arrival time of the surface wave on the negative component. (b) Example waveform disturbed by the Kyushu microseism: symmetric component cross-correlation in which the positive and negative components in (a) are averaged. (c) Example waveform undisturbed by the Kyushu microseism: positive component of the cross-correlation in (a). (d) & (e) Frequency-time (group velocity) diagrams from (b) and (c), respectively. (f) Comparison between the group velocity curves of cross-correlations shown in (b) and (c). Red triangles and stars are the phase and the group velocity curves waveforms in (b). Blue symbols show the group and phase velocity curves of the undisturbed signal.

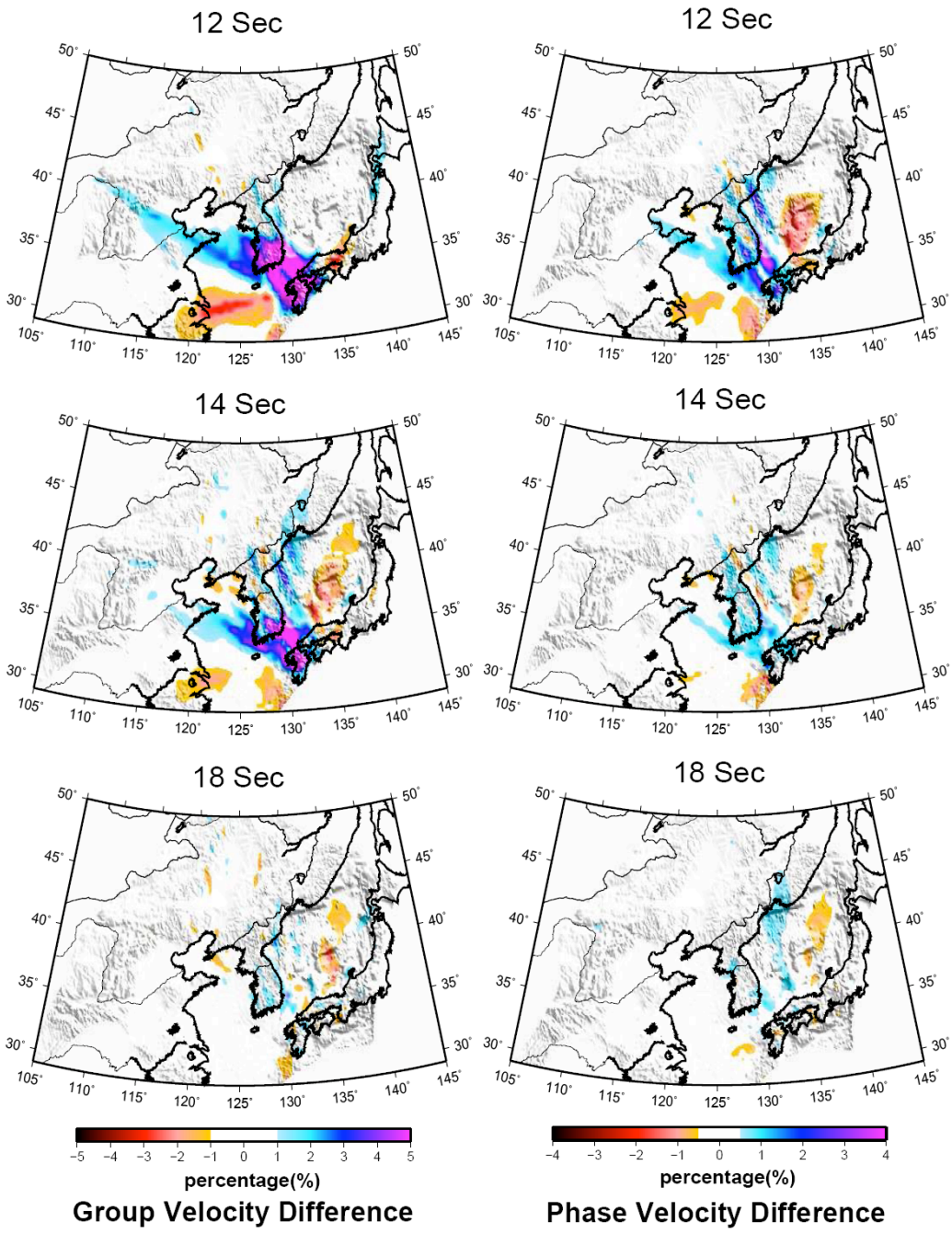

Figure 7. Estimates of the effect of the persistent Kyushu microseism on the phase and group velocity maps. The left column shows the differences between the group velocity maps at periods of 12, 14, and 18 sec based on the original data compared with the data in which the Kyushu signal has been removed. The right column shows similar differences for phase velocity. The effect of the Kyushu signal is stronger on group than phase velocity and at periods between 8 and 14 sec .

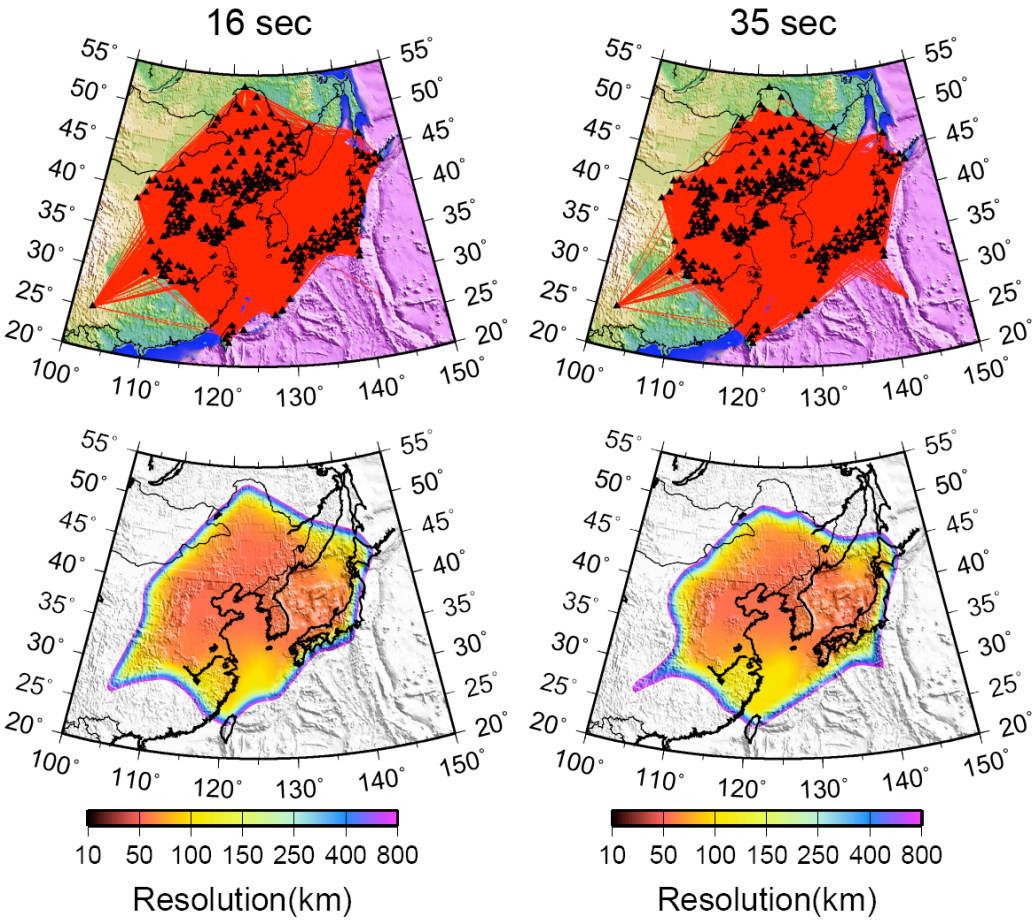

Figure 8. Ray path coverage (top) and resolution (bottom) at periods of 16 and 35 sec. Resolution is presented in units of km and is defined as twice the standard deviation of a 2-D Gaussian fit to the resolution surface at each geographic node (Barmin et al. 2001).

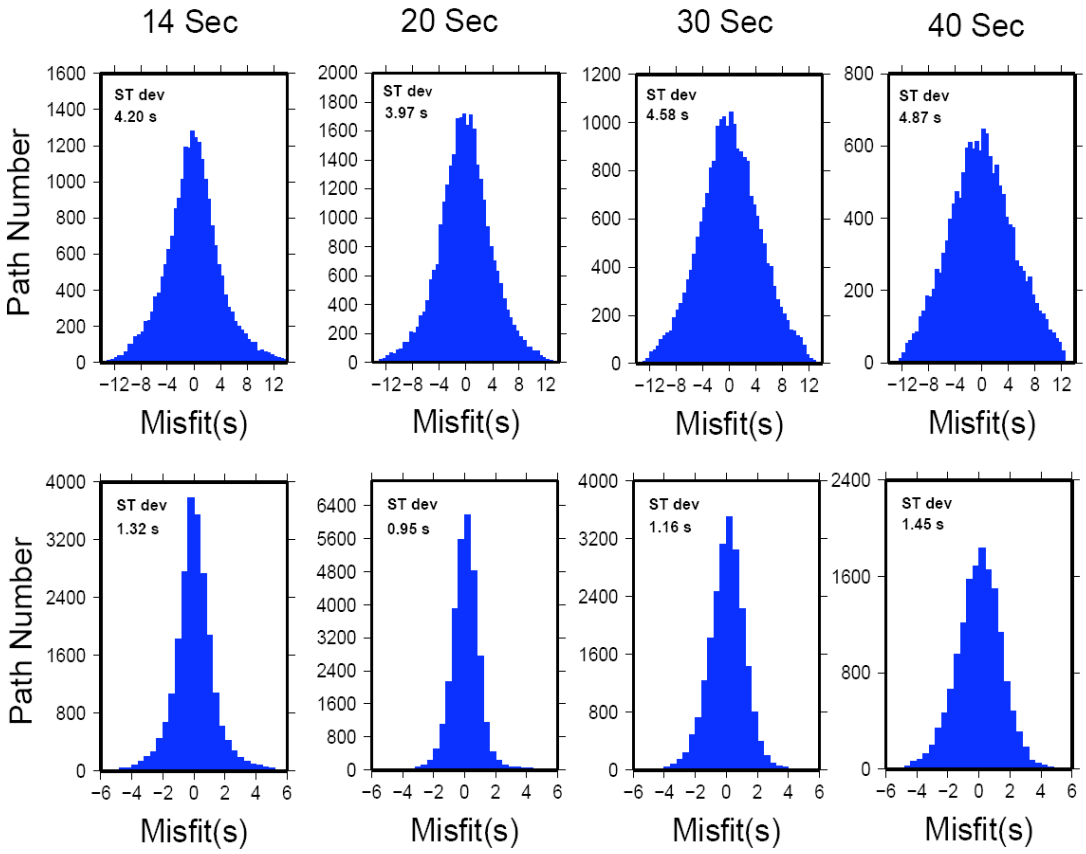

Figure 9. Misfit histograms at periods 14, 20, 30, and 40 sec, respectively. The top figures show the group velocity misfit and the lower figures are the phase velocity misfits. The standard deviations are shown on each panel.

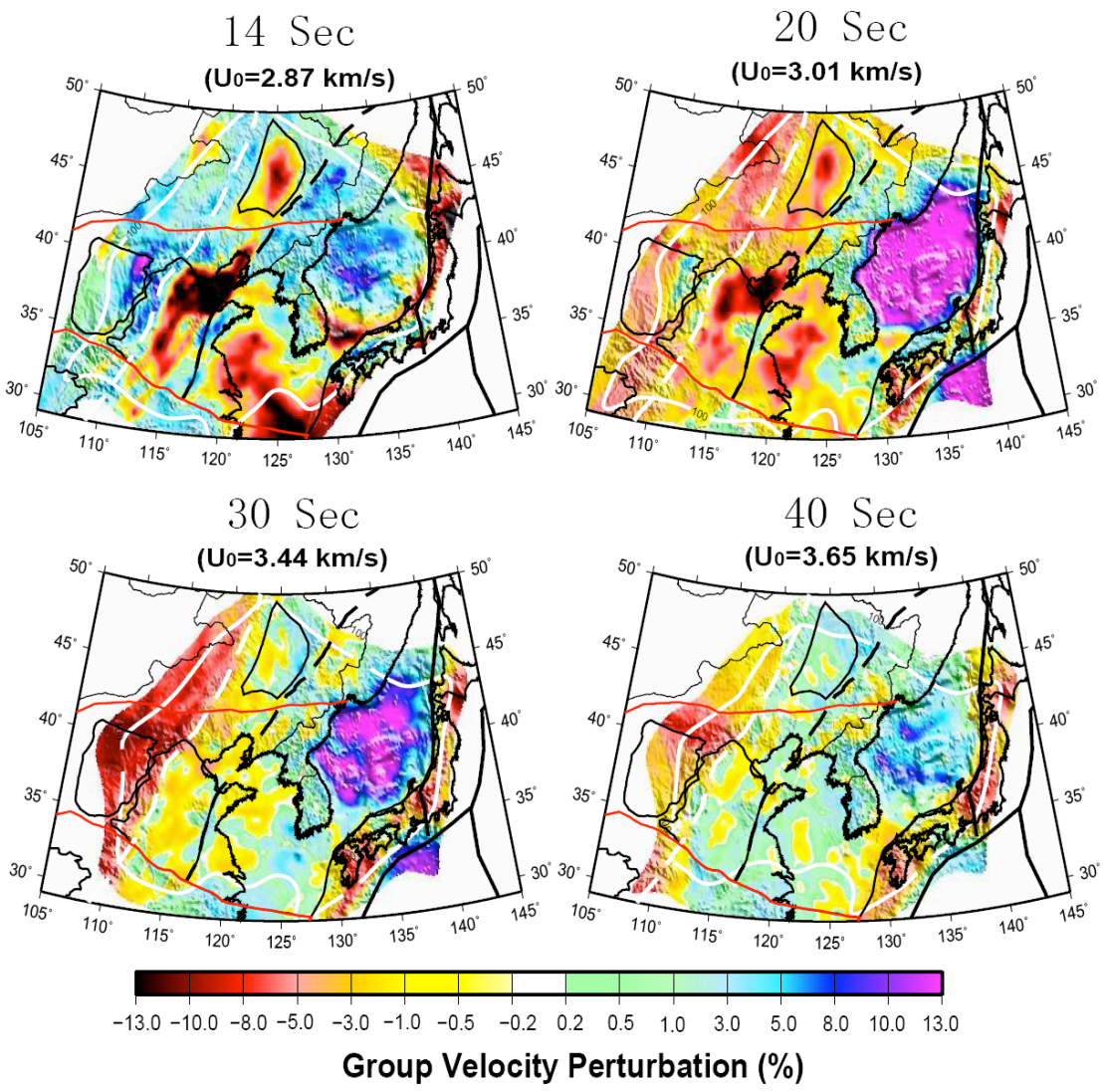

Figure 10. Group velocity maps at periods of 14, 20, 30, and 40 sec. Group velocities are plotted as perturbations relative to the average velocity (U_0) within the 400 km resolution contour. Only areas with spatial resolution better than 400 km are shown and the thick white line is the 100 km resolution contour. Other lines show tectonic and geological boundaries and are identified in Fig. 2.

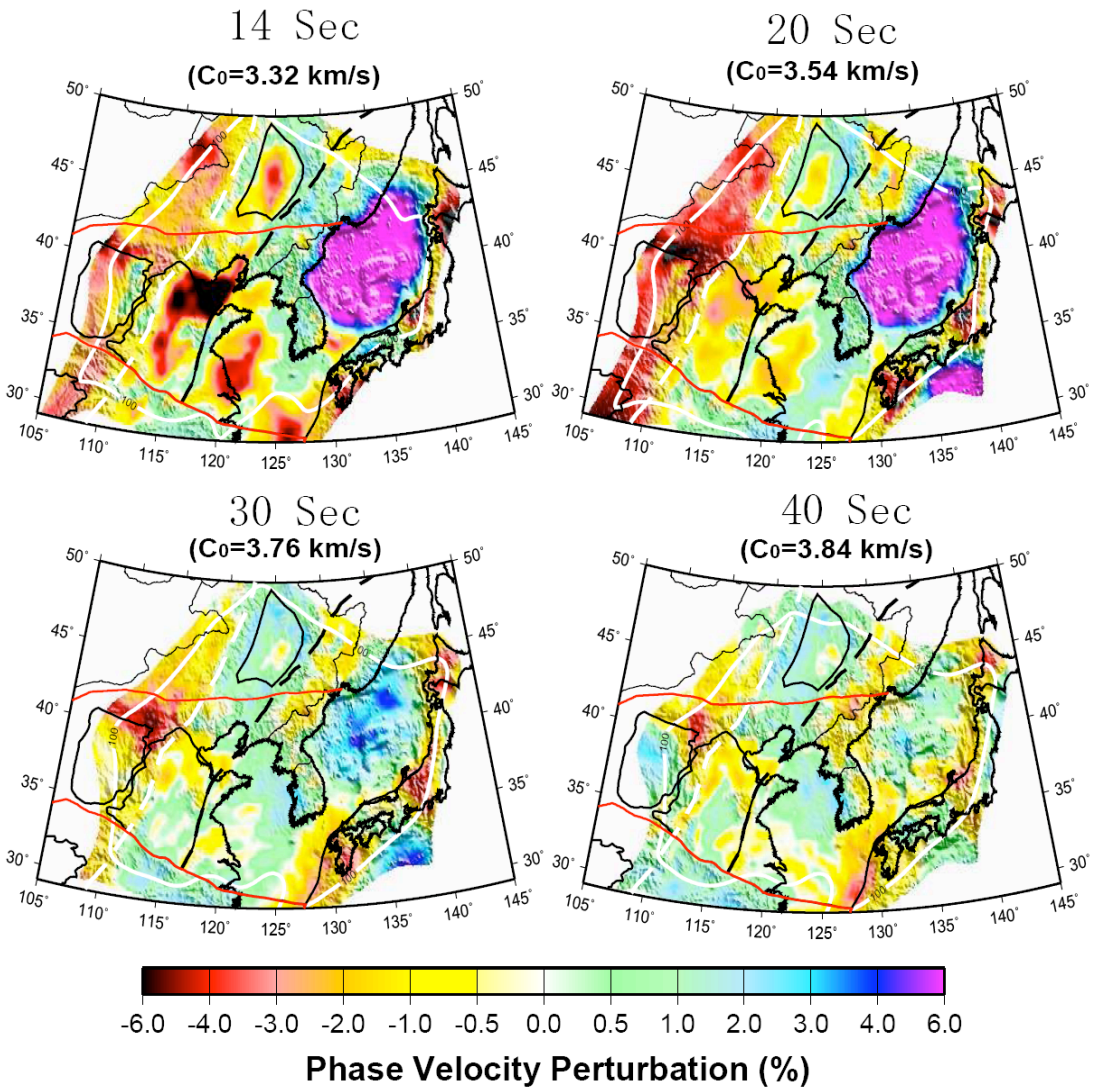

Figure 11. Same as Fig. 10, but for phase velocity maps at periods of 14, 20, 30 and 40 sec.

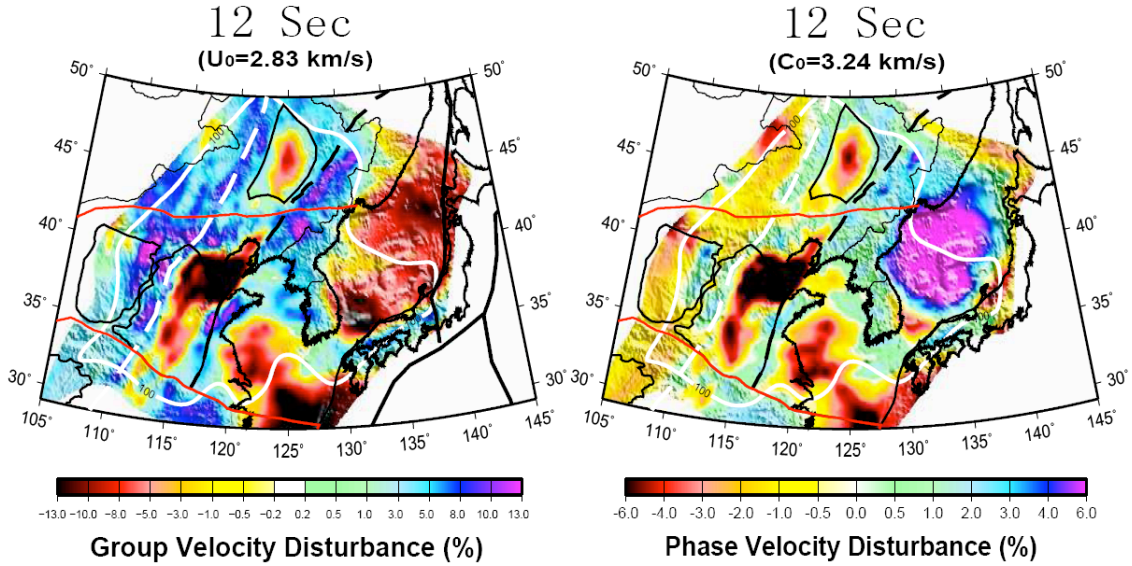

Figure 12. Same as Figs. 10 and 11, but for group and phase velocity maps at 12 sec period.

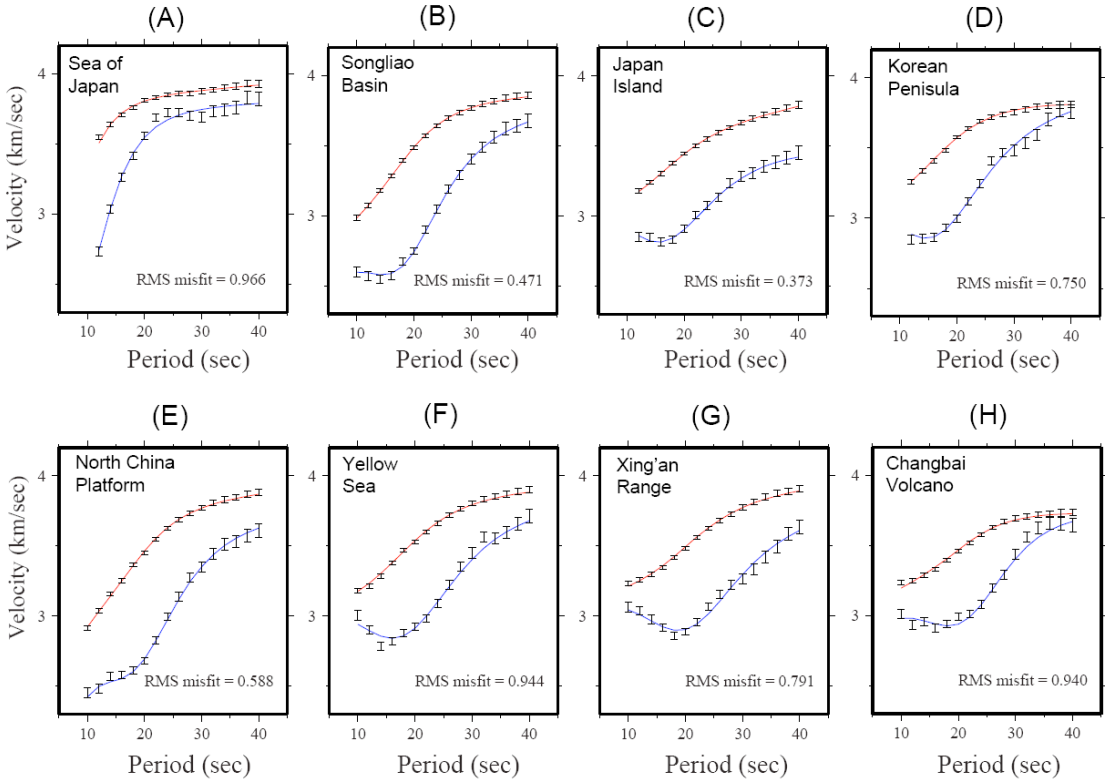

Figure 13. Phase (red lines) and group (blue lines) velocity curves at the eight selected locations shown in Fig. 2. The dispersion curves are predicted by the center of the ensemble of models at each location shown in Fig. 14. The error bars are twice the average uncertainties determined via eikonal tomography in the western US. The RMS misfits are calculated by equation (1).

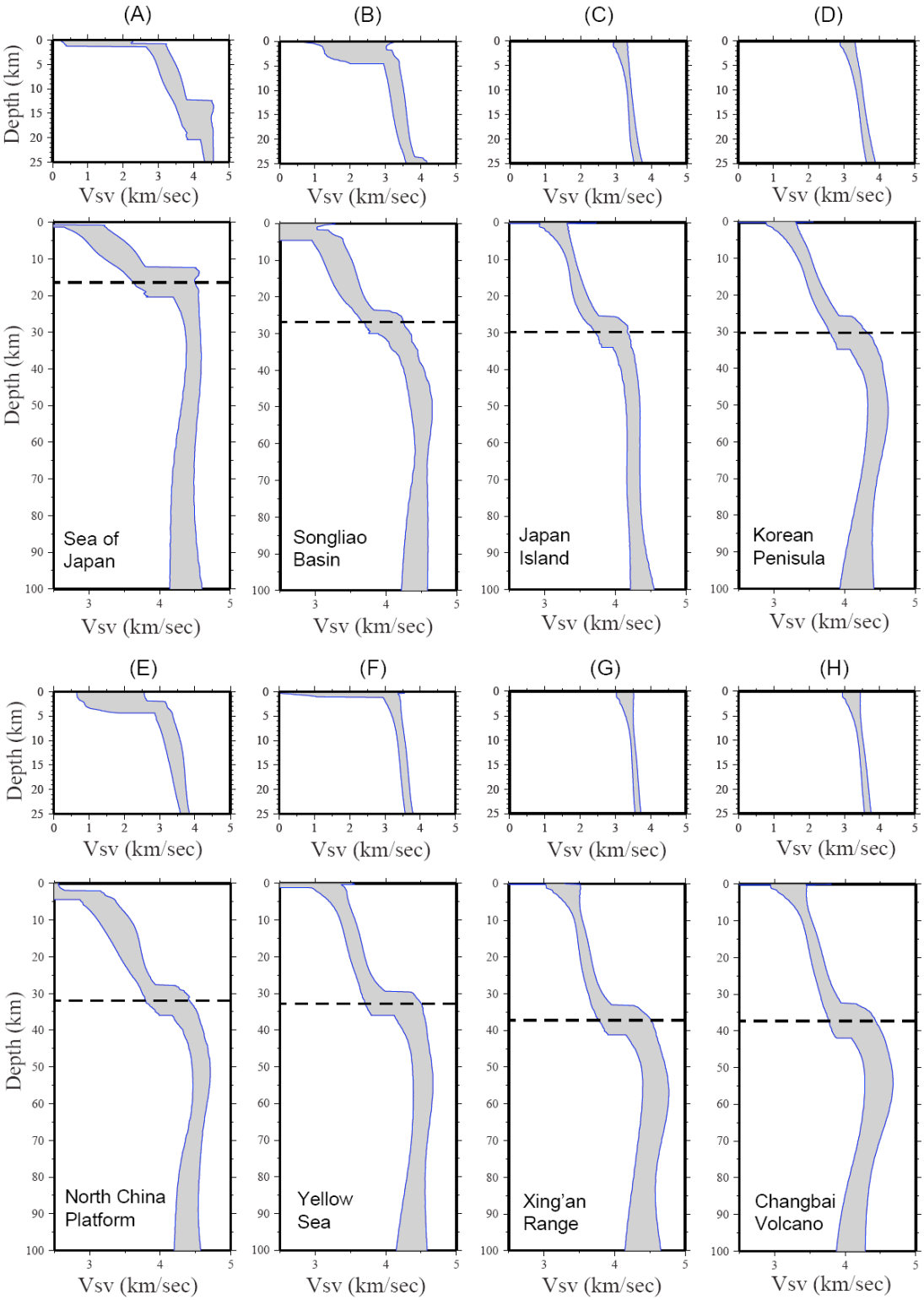

Figure 14. Shear wave (V_{sv}) velocity structures at the eight selected locations shown in Figure 2. The model at each location is shown as a pair in which each upper panel illustrates the crustal structure from the surface to a depth of 25 km and the lower panel shows the crustal and the uppermost mantle structure. The gray corridor is the 2σ (st dev) uncertainty and the dashed lines in each lower panel is the crustal thickness at each point.